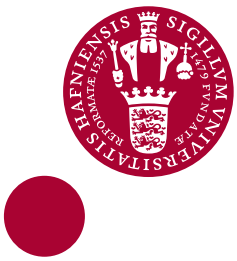

Starbursts in and out of the star-formation main sequence

Elbaz, D.; Leiton, R.; Nagar, N.; Okumura, K.; Franco, M.; Schreiber, C.; Pannella, M.; Wang, T.; Dickinson, M.; Diaz-Santos, T.; Ciesla, L.; Daddi, E.; Bournaud, F.; Magdis, G.; Zhou, L.; Rujopakarn, W.

Published in:
Astronomy & Astrophysics

DOI:
10.1051/0004-6361/201732370

Publication date:
2018

Document version
Publisher's PDF, also known as Version of record

A&A 616, A110 (2018)
https://doi.org/10.1051/0004-6361/201732370

Astronomy & Astrophysics

Starbursts in and out of the star-formation main sequence

D. Elbaz[1], R. Leiton[2,3,1], N. Nagar[2], K. Okumura[1], M. Franco[1], C. Schreiber[4,1], M. Pannella[5,1], T. Wang[1,6], M. Dickinson[7], T. Díaz-Santos[8], L. Ciesla[1], E. Daddi[1], F. Bournaud[1], G. Magdis[9,10], L. Zhou[1,11], and W. Rujopakarn[12,13,14]

[1] Laboratoire AIM-Paris-Saclay, CEA/DRF/Irfu – CNRS – Université Paris Diderot, CEA-Saclay, pt courrier 131, 91191 Gif-sur-Yvette, France
e-mail: delbaz@cea.fr
[2] Department of Astronomy, Universidad de Concepción, Casilla 160 Concepción, Chile
[3] Instituto de Física y Astronomía, Universidad de Valparaíso, Avda. Gran Bretaña 1111, Valparaíso, Chile
[4] Leiden Observatory, Leiden University, 2300 RA Leiden, The Netherlands
[5] Fakultät für Physik der Ludwig-Maximilians-Universität, 81679 München, Germany
[6] Institute of Astronomy, The University of Tokyo, 2-21-1 Osawa, Mitaka, Tokyo 181-0015, Japan
[7] National Optical Astronomy Observatory, 950 North Cherry Ave., Tucson, AZ 85719, USA
[8] Núcleo de Astronomía de la Facultad de Ingeniería, Universidad Diego Portales, Av. Ejército Libertador 441, Santiago, Chile
[9] Dark Cosmology Centre, Niels Bohr Institute, University of Copenhagen, Juliane Mariesvej, 30-2100 Copenhagen, Denmark
[10] Institute for Astronomy, Astrophysics, Space Applications and Remote Sensing, National Observatory of Athens, 15236 Athens, Greece
[11] School of Astronomy and Space Science, Nanjing University, Nanjing 210093, PR China
[12] Department of Physics, Faculty of Science, Chulalongkorn University, 254 Phayathai Road, Pathumwan, Bangkok 10330, Thailand
[13] National Astronomical Research Institute of Thailand (Public Organization), Donkaew, Maerim, Chiangmai 50180, Thailand
[14] Kavli Institute for the Physics and Mathematics of the Universe (WPI), The University of Tokyo Institutes for Advanced Study, The University of Tokyo, Kashiwa, Chiba 277-8583, Japan

Received 27 November 2017 / Accepted 15 April 2018

ABSTRACT

Aims. We use high-resolution continuum images obtained with the Atacama Large Millimeter Array (ALMA) to probe the surface density of star formation in $z \sim 2$ galaxies and study the different physical properties between galaxies within and above the star-formation main sequence of galaxies.
Methods. We use ALMA images at 870 μm with 0.2 arcsec resolution in order to resolve star formation in a sample of eight star-forming galaxies at $z \sim 2$ selected among the most massive *Herschel* galaxies in the GOODS-*South* field. This sample is supplemented with eleven galaxies from the public data of the 1.3 mm survey of the *Hubble* Ultra-Deep Field, HUDF. We derive dust and gas masses for the galaxies, compute their depletion times and gas fractions, and study the relative distributions of rest-frame ultraviolet (UV) and far-infrared (FIR) light.
Results. ALMA reveals systematically dense concentrations of dusty star formation close to the center of the stellar component of the galaxies. We identify two different starburst regimes: (i) the classical population of starbursts located above the SFR-$M_\star$ main sequence, with enhanced gas fractions and short depletion times and (ii) a sub-population of galaxies located within the scatter of the main sequence that experience compact star formation with depletion timescales typical of starbursts of ~150 Myr. In both starburst populations, the FIR and UV are distributed in distinct regions and dust-corrected star formation rates (SFRs) estimated using UV-optical-near-infrared data alone underestimate the total SFR. Starbursts hidden in the main sequence show instead the lowest gas fractions of our sample and could represent the last stage of star formation prior to passivization. Being *Herschel*-selected, these main sequence galaxies are located in the high-mass end of the main sequence, hence we do not know whether these "starbursts hidden in the main sequence" also exist below 10^{11} $M_\odot$. Active galactic nuclei (AGNs) are found to be ubiquitous in these compact starbursts, suggesting that the triggering mechanism also feeds the central black hole or that the active nucleus triggers star formation.

Key words. galaxies: evolution – galaxies: starburst – galaxies: active – galaxies: formation – galaxies: star formation – submillimeter: galaxies

1. Introduction

During the 6 billion years that passed between a redshift of $z \sim 2.5$ and 0.5, galaxies formed 75% of their present stellar mass (see Fig. 11 of Madau & Dickinson 2014) following a star-formation mode in which most of the ultraviolet (UV) starlight was absorbed by interstellar dust and re-radiated in the mid- to far-infrared (MIR and FIR, respectively, see e.g., Le Floc'h et al. 2005; Magnelli et al. 2009, 2013; Burgarella et al. 2013; Madau & Dickinson 2014 and references therein).

The galaxies that contributed most to the cosmic star formation rate (SFR) density therefore radiated most of their light in the infrared (IR) domain and at the peak epoch of cosmic star formation, the so-called "cosmic noon" around $z \sim 2$; these galaxies belonged to the class of luminous and ultraluminous infrared galaxies; LIRGs and ULIRGs ((U)LIRGs hereafter) respectively,

with total infrared luminosities of $L_{\rm IR} = 10^{11}$–10^{12} $L_\odot$ and $L_{\rm IR} > 10^{12}$ $L_\odot$, respectively. It is therefore, of prime importance to understand the star-formation mode of $z \sim 2$ dusty star-forming galaxies to trace the origin of present-day stars and galaxies.

Contrary to their local siblings, the distant (U)LIRGs do not systematically exhibit the signature of merger-driven starbursts with compact star formation and depletion times of the order of ∼150 Myr. Instead, the majority of them appear to be forming stars through a secular mode of star formation (see e.g., Elbaz et al. 2010, 2011; Daddi et al. 2010b; Rujopakarn et al. 2011; Wuyts et al. 2011b) with depletion times, $\tau_d = M_{\rm gas}/SFR \sim$ 600 Myr (Tacconi et al. 2018). Here, τ_d is the time it would take for the galaxy to exhaust its molecular gas reservoir assuming a constant SFR. It is the inverse of the star formation efficiency (SFE). This evolution from a local population of rare violent merger-driven local (U)LIRGs to a common population of secularly evolving star-forming galaxies at $z \sim 2$ is for the most part a natural result of the fast rise of the gas fraction of (U)LIRGs with increasing redshift (see e.g., Daddi et al. 2010a; Tacconi et al. 2010, 2018; Magdis et al. 2012b).

This change in the nature of (U)LIRGs as a function of cosmic time can also be seen in the framework of the global evolution of the correlation between the SFR and stellar mass followed by star-forming galaxies, the so-called "star-formation main sequence" (MS, hereafter). This tight correlation between the SFR and stellar mass ($M_\star$) is followed by the majority of star-forming galaxies from $z \sim 0$ up to at least $z \sim 3.5$ (Elbaz et al. 2007; Noeske et al. 2007; Daddi et al. 2007; Pannella et al. 2009, 2015; Karim et al. 2011; Wuyts et al. 2011a; Whitaker et al. 2012, 2014; Rodighiero et al. 2014; Renzini & Peng 2015; Schreiber et al. 2015, 2017). While the existence of a correlation between SFR and $M_\star$ is natural, the fact that 68% of the star-forming galaxies of a given stellar mass formed their stars with the same SFR within a factor 2 (0.3 dex–RMS) during 85% of cosmic history (Schreiber et al. 2015) does appear as a surprise and a challenge for models.

This implies, in particular, that galaxies more massive than $M_\star = 10^{10}$ $M_\odot$ were LIRGs and galaxies with $M_\star \geq 1.4 \times 10^{11}$ $M_\odot$ were ULIRGs at $z \sim 2$. (U)LIRGs therefore represented a common phase among distant massive galaxies and studying their nature is equivalent to studying the origin of massive galaxies. Indeed, the studies of the dust and gas content of $z \sim 2$ star-forming galaxies revealed much longer typical depletion times for MS galaxies at all masses, including (U)LIRGs at the high-mass end of the MS which also present depletion times of about 600 Myr (Magdis et al. 2012b, Genzel et al. 2015; Béthermin et al. 2015; Tacconi et al. 2018).

The existence of a SFR – $M_\star$ MS is commonly used to disentangle a secular–universal star-formation mode of galaxies within the MS from a stochastic star-formation mode of galaxies out of the MS, in which starbursts systematically lie above the MS (see e.g., Rodighiero et al. 2011; Elbaz et al. 2011; Schreiber et al. 2015 and references therein). The fact that the proportion of starbursts – defined as galaxies experiencing star formation three or four times above the median of the MS SFR – remains limited to a few percent at all redshifts and masses (Rodighiero et al. 2011; Schreiber et al. 2015) is puzzling when one considers that the observed (e.g., Kartaltepe et al. 2007) and modeled (e.g., Hopkins et al. 2010) merger rates rapidly rise with increasing redshift.

What physical processes sustain the secular star-formation of the MS? What role did mergers play around cosmic noon? Are starbursts limited to the small population of galaxies with an extremely large specific SFR (sSFR = SFR/$M_\star$, e.g., Rodighiero et al. 2011) or can there be starbursts "hidden" within the MS? Should one interpret the MS of star-forming galaxies as evidence that galaxies within it unequivocally form their stars following a common universal mode that is, in particular, unaffected by mergers?

We address these questions in this paper by taking advantage of the exquisite angular resolution of the Atacama Large Millimeter Array (ALMA). We use ALMA to probe the distribution of dusty star formation in $z \sim 2$ (U)LIRGs and compare it with that derived from rest-frame UV light. We compare the spatial locations of UV-transparent and dusty star formation and discuss the presence or absence of spatial correlations between both with other galaxy properties, such as their depletion time and star-formation compactness. Here we identify a population of galaxies that lie within the MS but that exhibit enhanced star formation typical of starbursts – in terms of star-formation efficiency, SFE = SFR/$M_{\rm gas}$, or equivalently depletion time, $\tau_{\rm dep} = 1/{\rm SFE}$. We consider several possible scenarios that may provide an explanation for the existence of these starbursts hidden in the MS, study a possible link with the presence of an active galactic nucleus (AGN) and discuss implications on the formation of compact early-type galaxies as observed at $z \sim 2$ (e.g., van der Wel et al. 2014).

Throughout this paper we use a Salpeter (1955) initial mass function (IMF), and adopt a ΛCDM cosmology with $\Omega_{\rm M} = 0.3$, $\Omega_\Lambda = 0.7$, and $H_0 = 70$ km s^{-1} Mpc^{-1} . As a matter of notation, we refer to the rest-frame GALEX far-ultraviolet (FUV) bandpass and to the total integrated IR light in the range 8–1000 μm when using the subscripts "UV" and "IR", respectively.

2. Data

An ensemble of 8 galaxies with *Herschel* photometry defines the core sample of this study for which deep 870 μm ALMA (band 7) continuum images were obtained (40–50 min on source, Cycle 1, P.I. R.Leiton). These galaxies are complemented with 11 galaxies observed at 1.3 mm from public ALMA data in the *Hubble* Ultra-Deep Field, HUDF ($\sigma_{1.3} \sim 35\,\mu$Jy; Rujopakarn et al. 2016; Dunlop et al. 2017). The resulting sample of 19 galaxies at $z \sim 2$ is described below.

2.1. Sample selection

The main sample of galaxies used for this paper comes from the ALMA project 2012.1.00983.S (PI R.Leiton, Cycle 1) which was observed from August 29 to September 1, 2014. It consists of eight $z \sim 2$ ULIRGs (ultra-luminous infrared galaxies, $L_{\rm IR} \geq 10^{12}$ $L_\odot$) that were selected from a sample of *Herschel* galaxies detected in the GOODS-*South* field from the GOODS-*Herschel* open time key program (Elbaz et al. 2011).

These galaxies were selected in such a way as to avoid being heavily biased towards the minor population of starburst galaxies well above the MS, but at the same time to reach a high enough signal-to-noise ratio (S/N) in the high-resolution ALMA images at 870 μm (i.e., 290 μm rest-frame). The image quality and resolution were set with the goal of being able to determine the compactness and clumpiness of star-formation in these galaxies. This resulted in the requirements listed below that limited the sample to only 8 galaxies with a median stellar mass of $M_\star = 1.9 \times 10^{11}$ $M_\odot$.

Table 1. ALMA sources.

ID	ID_{CLS}	RA_{CLS}, Dec_{CLS} 3h 32m...,−27°...	Offset arcsec
(1)	(2)	(3)	(4)
GS1	3280	14.55 s, 52′56.54″	0.176,−0.188
GS2	5339	54.69 s, 51′40.70″	0.052,−0.232
GS3	2619	39.25 s, 53′25.71″	0.083,−0.173
GS4	7184	17.21 s, 50′37.07″	0.161,−0.280
GS5	9834	35.72 s, 49′16.04″	0.089,−0.248
GS6	14 876	28.51 s, 46′58.14″	0.091,−0.269
GS7	8409	37.74 s, 50′00.41″	0.067,−0.225
GS8	5893b	46.84 s, 51′21.12″	0.081,−0.184
UDF1	15 669	44.03 s, 46′35.70″	0.066,−0.277
UDF2	15 639	43.53 s, 46′39.00″	0.057,−0.277
UDF3	15 876	38.54 s, 46′34.06″	0.083,−0.243
UDF4	15 844	41.03 s, 46′31.45″	0.063,−0.250
UDF5	13 508	36.97 s, 47′27.21″	0.101,−0.239
UDF6	15 010	34.43 s, 46′59.57″	0.100,−0.254
UDF7	15 381	43.32 s, 46′46.80″	0.050,−0.250
UDF8	16 934	39.74 s, 46′11.25″	0.043,−0.289
UDF11	12 624	40.05 s, 47′55.46″	0.090,−0.242
UDF13	15 432	35.08 s, 46′47.58″	0.098,−0.260
UDF16	14 638	42.38 s, 47′07.61″	0.069,−0.242

Notes. The upper part of the table lists the 8 galaxies (GS1 to GS8) observed with ALMA at 870 μm at a 0.2 arcsec resolution in our ALMA program. The lower part lists the 11 galaxies (UDF#) from the 1.3 mm ALMA survey of the HUDF by Dunlop et al. (2017) at a resolution of 0.35 arcsec. Column (1) simplified ID. For the UDF galaxies, we use the same IDs as in Dunlop et al. (2017). Columns (2) and (3) CANDELS ID and coordinates from Guo et al. (2013). GS8, initially associated with the galaxy with the CANDELS ID 5893, was found to be associated with a background galaxy that we will call 5893b (see Sect. 3.1). Column (4) offset to be applied to the HST CANDELS coordinates to match the ALMA astrometry.

Starting from the GOODS-*Herschel* galaxy catalog (described in Elbaz et al. 2011), we selected the ALMA targets under the following conditions:

(i) A redshift – either spectroscopic or photometric – of $1.5 < z < 2.6$ to ensure that the MIPS-24 μm band encompasses the 8 μm wavelength to allow the determination of a rest-frame 8 μm luminosity, necessary to compute the *IR*8 color index. This color index, $IR8 = L_{\rm IR}/L_{8\mu{\rm m}}$, was found to exhibit a tight correlation with the surface density of mid and far-infrared luminosity by Elbaz et al. (2011). Here $L_{8\mu{\rm m}}$ is the νL_ν broadband luminosity integrated in the *Spitzer*–IRAC band 4 centered at 8 μm and $L_{\rm IR}$ is the total infrared luminosity integrated from 8 to 1000 μm. *IR*8 provides an independent tracer of dusty star formation compactness. This redshift encompasses the key epoch of interest here, the cosmic noon of the cosmic SFR density, and is large enough to bring the central wavelength, 870 μm, of ALMA band 7 (345 GHz) close to the peak of the far-infrared emission.

(ii) A sampling of the FIR spectral energy distribution (SED) with measurements in at least four FIR bands (100, 160, 250, 350 μm). This requirement is mainly constrained by the condition to have a 3σ detection in the 250 and 350 μm bands together with the condition that the *Herschel*–SPIRE measurements are not heavily affected by contamination from close neighbors. The latter condition is determined through the use of a "clean index" (defined in Elbaz et al. 2010, 2011). The clean index is used to reject sources with highly uncertain flux densities due to confusion by only selecting sources with at most one neighbor closer than $0.8 \times FWHM$ (250 μm) = 18″ and brighter than half the 24 μm flux density of the central object. This was done using the list of sources detected at 24 μm above 20 μJy. Simulations using realistic IR SED and galaxies spatial distributions together with the *Herschel* noise showed that this criterion ensures a photometric accuracy better than 30% in at least 68% of the cases for SPIRE detections (Leiton et al. 2015).

(iii) We rejected sources with unphysical SEDs, that is, for which one or more of the flux densities from 24 to 350 μm presented a nonphysical jump. This smoothness condition on the SED was required to reject sources with blending effects, affecting mainly the longest *Herschel* wavelengths even after imposing the clean index criterion.

For the sake of simplicity, we labeled the eight sources GS1 to GS8. We also provide their CANDELS ID, ID_{CLS}, from Guo et al. (2013) in Table 1. We note that all of the *Herschel* sources studied here were found to be associated with a single ALMA source, none were resolved into two or more ALMA sources.

2.2. Supplementary sample from the Hubble Ultra Deep Field

We supplemented our sample with a reference sample of galaxies detected with ALMA at 1.3 mm with a resolution of ~0.35 arcsec within the 4.5 arcmin^2 survey of the *Hubble* Ultra Deep Field (HUDF) down to $\sigma_{1.3} \sim$ 35 μJy (see Rujopakarn et al. 2016; Dunlop et al. 2017). We use here the 11 galaxies listed in Table 2 of Rujopakarn et al. (2016; see Sect. 2.3). The galaxies are labeled UDF# in Table 1 as in Dunlop et al. (2017).

2.3. ALMA observations and data reduction

2.3.1. ALMA observations

Each one of the eight targeted galaxies was observed with a single pointing with a total of 36 antennas in band 7 (345 GHz, 870 μm) at an angular resolution of 0.2″(ALMA synthesized beam of 0.2″ × 0.16″). The integration time on each science target ranges from 37 to 50 min, resulting in typical S/Ns at 870 μm of $S/N \sim 35$ and up to 75 for the brightest one. The integration time was defined in order to reach a minimum $S/N = 10$ on 20% of the predicted 870 μm ALMA flux density (extrapolated from *Herschel*) or equivalently 50 σ on the total flux in order to be able to measure an effective radius even for the most compact galaxies and to individually detect the major clumps of star formation when they exist and produce at least 20% of the total ALMA flux density. For the typical predicted flux density of $F_{870} \sim$ 2.5 mJy of the sample, this led to a total observing time of at least 35 min/object. Accounting for the predicted flux densities of the galaxies, we used slightly different integration times of 36.5, 38.8, and 49.5 min (excluding overheads) for [GS4, GS5, GS6, GS8], [GS1, GS7], and [GS2, GS3], respectively. The observed standard deviation of the noise spans $rms = 40$–$70\,\mu$Jy. Accounting for the obtained S/N, the accuracy on the size measurements given by CASA corresponds to $FWHM/\sqrt{(S/N)} \sim 0.034$ arcsec that represents a theoretically expected precision, if we assume that the sources have a Gaussian profile, corresponding to ~280 pc at $z \sim 2$.

2.3.2. Data reduction, flux, and size measurements

The data reduction was carried out with CASA, and the final images were corrected for the primary beam, although all our targets are located at the center of the ALMA pointings. Flux densities and sizes were both measured in the *uv*-plane, using the "uvmodelfit" code in CASA, and in the image plane using the GALFIT code (Peng et al. 2002). Since uvmodelfit only allows 2D Gaussian profile fitting, we computed Gaussian and Sérsic profiles with GALFIT to compare both results. The Gaussian semi-major axis ($R_{1/2} = 0.5 \times FWHM$ of the major axis) derived in the *uv*-plane and image plane – with uvmodelfit and GALFIT respectively – agree within 15%, with only a 5% systematic difference (larger sizes in the GALFIT measurements in the image plane). However, the uncertainties estimated by GALFIT in the image plane are 45% smaller (median, with values that can reach more than a factor 2). We consider that the uncertainties measured in the *uv*-plane are most probably more realistic, and in any case more conservative, hence we have decided to use the uvmodelfit measurements for our analysis (see Table 2).

We compared the Gaussian semi-major axis from uvmodelfit, $R_{1/2}$, with the effective radius, R_e, obtained with a Sérsic profile fit either leaving the Sérsic index free, $n^{\rm Sersic}_{ALMA}$, or imposing $n^{\rm Sersic}_{ALMA} = 1$ (exponential disk profile). We find that $R_{1/2}$ and R_e agree within 20% in both cases with no systematic difference when imposing $n^{\rm Sersic}_{ALMA} = 1$ and 4% smaller sizes when the Sérsic index is left free. We obtain a S/N greater than 3 for the Sérsic indices (Col. (7) in Table 2) of all the GS sources except GS2 and GS3 (ID CANDELS 5339 and 2619).

Therefore, even though we did perform Sérsic profile fittings and determined $n^{\rm Sersic}_{ALMA}$, the light distribution of our galaxies does not seem to show very strong departure from a 2D Gaussian. As a result, both $R_{1/2}$ and R_e provide an equally good proxy for the half-light radius, encompassing 50% of the IR luminosity. We did measure some moderate asymmetries quantified by the minor (b) over major (a) axis ratio, b/a (Col. (5) in Table 2) that we used to derive circularized half-light radii, R^{circ}_{ALMA} (listed in kpc in the Col. (6) of Table 2) following Eq. (1).

$$R^{circ}_{ALMA}[\mathrm{kpc}] \;=\; R_{1/2} \times \sqrt{\frac{b}{a}} \times \mathrm{Conv}(''\,\mathrm{to\,kpc}). \qquad (1)$$

Conv(″ to kpc) is the number of proper kpc at the redshift of the source and is equal to 8.46, 8.37, and 8.07 kpc/″at $z = 1.5$, 2, and 2.5, respectively. We then used R^{circ}_{ALMA} – that encompasses 50% of the IR luminosity – to compute the IR luminosity surface densities of our galaxies as in Eq. (2).

$$\Sigma_{\rm IR}\left[L_\odot\ \mathrm{kpc}^{-2}\right] \;=\; \frac{L_{\rm IR}/2}{\pi\left(R^{circ}_{ALMA}\right)^2}. \qquad (2)$$

The sizes of the HUDF galaxies were measured as well using a 2D elliptical Gaussian fitting by Rujopakarn et al. (2016) who used the PyBDSM[1] code. We analyzed the public ALMA image of the HUDF and found that the quality of the images did not permit us to constrain both a Sérsic effective radius and index, hence we do not provide Sérsic indices for the HUDF galaxies. Using GALFIT, we fitted 2D Gaussian elliptical profiles on the 11 HUDF sources listed in Rujopakarn et al. (2016) and found a good agreement between our measured Gaussian FWHM values and those quoted in Rujopakarn et al. (2016) with a median ratio of exactly 1 and an RMS of 16% for the sources with $S/N > 5$. Below this threshold, the measured sizes agree within the error bars which start to be quite large. The sizes listed in Rujopakarn et al. (2016) are quoted in Table 2.

The flux densities of the GS galaxies were computed using our 2D elliptical Gaussian fitting in the *uv*-plane. For the HUDF galaxies, they correspond to those listed in Rujopakarn et al. (2016) consistent with our own measurements.

[1] http://www.astron.nl/citt/pybdsm

2.3.3. ALMA versus HST astrometry

The ALMA and HST coordinates present a small systematic offset in the GOODS-*South* field. This offset does not exist between ALMA and other observatories such as 2MASS, JVLA, *Gaia*, or Pan-STARRS but it affects the astrometry of the HST sources. A comparison of the positions of HST sources in the HUDF with 2MASS (Dunlop et al. 2017) and JVLA (Rujopakarn et al. 2016) showed that the HST positions needed to be corrected by −0.26 arcsec in Declination and +0.08 arcsec in Right Ascension. This implies that the HST coordinates (in decimal degrees) must be systematically corrected by $[+2.51, -7.22] \times 10^{-5}$ degree (including the cos(δ) factor).

This offset is too small to change the HST counterparts of the ALMA detections. However, it has an impact on the detailed comparison of the location and shape of the ALMA millimeter emission with that of the HST optical light that will be discussed in the following sections. Hence we decided to extend further our analysis of this astrometric issue by searching for possible local offsets added to the global one mentioned above. A detailed description of the resulting analysis will be presented in Dickinson et al. (in prep.). We just briefly summarize here the main lines of this process and its implications on our analysis.

The main reasons for this astrometric issue can be traced back to the astrometric references that were used to build the HST mosaics of the GOODS-*South* field. At the time, the astrometric reference used for GOODS-*South* was an ESO 2.2 m Wide Field Imager (WFI) image, itself a product of a combination of different observing programs (the ESO Imaging Survey, EIS and COMBO-17 among others). The GOODS HST team subsequently re-calibrated the WFI astrometry to match the HST Guide Star Catalog (GSC2).

More modern astrometric data are now available in this field such as Pan-STARRS1 (Chambers et al. 2016). We used the PanStarr DR1 catalog provided by Flewelling et al. (2016) to search for possible offsets in the different regions of the whole $10' \times 15'$ GOODS-*South* field.

We found residual distortions that we believe to be due to some combination of distortions in the WFI mosaic images and in the GSC2 positions, and zonal errors registering the HST ACS images to the WFI astrometry. These residual local distortions are plotted in Fig. 1 after having corrected the HST positions for the global offset mentioned above and marked with the open blue triangle. The distortion pattern was determined using a 2.4 arcmin diameter circular median determination of the offset in order to avoid artificial fluctuations due to the position uncertainty on the individual objects. This pattern was then applied to the 34, 930 HST WFC3-*H* sources of the CANDELS catalog in GOODS-*South* (Guo et al. 2013; shown as gray dots in Fig. 1).

The 11 galaxies detected by ALMA in the HUDF are all well centered on this position with residual offsets of the order of 0.02″(large filled purple dots). These extra corrections are truly negligible, since they correspond to 160 pc at the redshifts of the sources. However, the 8 GS galaxies are spread over a wider area in GOODS-*South* including parts where the residual offsets can

Table 2. Galaxy properties derived from the ALMA and HST–WFC3 H band (1.6 μm) data.

ID	z	F_{ALMA} (μJy)	$R_{1/2maj}$ (arcsec)	b/a	R^{circ}_{ALMA} (kpc)	$n^{\rm Sersic}_{ALMA}$	R^{circ}_{H} (kpc)	$n^{\rm Sersic}_{H}$	$\Sigma^{(a)}_{\rm IR}$ ($\times 10^{11} L_\odot$ kpc^{-2})	$IR8$
(1)	(2)	(3)	(4)	(5)	(6)	(7)	(8)	(9)	(10)	(11)
GS1	2.191	1190 ± 120	0.145 ± 0.016	0.72	0.87 ± 0.09	0.63 ± 0.18	0.73	3.75	3.73 ± 1.00	9.3 ± 0.8
GS2	2.326	1100 ± 70	0.163 ± 0.031	0.87	1.16 ± 0.22	1.07 ± 0.99	1.90	0.72	2.63 ± 1.21	7.2 ± 0.9
GS3	2.241	1630 ± 70	0.150 ± 0.016	0.42	0.52 ± 0.05	4.69 ± 1.65	2.81	2.03	14.96 ± 3.90	8.1 ± 0.6
GS4	1.956^{sp}	2100 ± 70	0.140 ± 0.010	0.82	0.97 ± 0.07	1.88 ± 0.59	3.93	1.77	3.54 ± 0.81	13.4 ± 1.8
GS5	2.576^{sp}	4420 ± 70	0.139 ± 0.006	0.92	1.03 ± 0.04	1.27 ± 0.22	2.57	1.08	10.12 ± 1.38	–
GS6	2.309^{sp}	5210 ± 70	0.120 ± 0.004	1.00	0.98 ± 0.03	1.15 ± 0.21	2.10	0.25	10.86 ± 1.27	27.3 ± 2.4
GS7	1.619^{sp}	2320 ± 70	0.194 ± 0.012	0.84	1.38 ± 0.09	1.78 ± 0.38	3.66	1.04	2.33 ± 0.41	19.8 ± 1.7
GS8	3.240	6420 ± 140	0.142 ± 0.003	0.62	0.67 ± 0.02	0.67 ± 0.04	1.63	3.53	20.86 ± 2.25	–
UDF1	3.000	924 ± 76	0.195 ± 0.020	0.85	1.24 ± 0.18	–	0.54	7.16	5.95 ± 2.00	–
UDF2	2.794^{sp}	996 ± 87	0.265 ± 0.030	0.85	1.77 ± 0.18	–	3.24	0.86	1.32 ± 0.33	–
UDF3	2.543^{sp}	863 ± 84	0.375 ± 0.045	0.36	1.59 ± 0.27	–	1.55	0.81	3.35 ± 1.28	9.9 ± 0.9
UDF4	2.430	303 ± 46	0.270 ± 0.060	0.52	1.42 ± 0.35	–	2.79	0.20	0.84 ± 0.47	7.9 ± 1.3
UDF5	1.759^{sp}	311 ± 49	0.480 ± 0.125	0.20	1.59 ± 0.62	–	2.24	0.71	0.48 ± 0.40	7.2 ± 0.7
UDF6	1.411^{sp}	239 ± 49	0.530 ± 0.205	0.19	1.77 ± 1.06	–	3.71	0.48	0.46 ± 0.58	–
UDF7	2.590	231 ± 48	0.120 ± 0.060	–	2.65 ± 1.33	–	4.24	0.77	0.25 ± 0.27	–
UDF8	1.546^{sp}	208 ± 46	0.675 ± 0.225	0.53	3.81 ± 1.24	–	5.57	3.04	0.11 ± 0.08	4.7 ± 0.4
UDF11	1.998^{sp}	186 ± 46	0.715 ± 0.285	0.48	3.72 ± 1.50	–	4.40	1.41	0.26 ± 0.22	6.4 ± 0.5
UDF13	2.497^{sp}	174 ± 45	0.430 ± 0.170	0.55	2.30 ± 0.97	–	1.14	1.86	0.22 ± 0.20	6.9 ± 1.3
UDF16	1.319^{sp}	155 ± 44	0.115 ± 0.058	–	2.74 ± 1.37	–	3.15	2.16	0.07 ± 0.07	–

Notes: Column (1) simplified ID. Column (2) photometric redshift, except for the galaxies marked with $^{(sp)}$ for which a spectroscopic redshift is available. Column (3) $F_{\rm ALMA}$ is the continuum flux density at 870 μm for the GS1 to GS8 sources and at 1.3 mm for the UDF1 to UDF16 sources. Columns (4) and (5) semi-major axis, $R_{1/2maj}$ in arcsec, and axis ratio, b/a, of the ALMA sources measured from uvmodelfit in CASA for the GS sources and from Rujopakarn et al. (2016) for the UDF galaxies. The consistency of the GS and UDF was checked in the direct images using GALFIT. The sizes of UDF7 and UDF16 are measured at the 2σ level. Column (6) circularized effective ALMA radius, $R^{circ}_{\rm ALMA}$, in kpc, as defined in Eq. (1). Column (7) Sérsic index, $n^{\rm Sersic}_{\rm ALMA}$, derived from the Sérsic fit to the ALMA 870 μm image for the GS sources using GALFIT on the direct images. The S/N of the UDF sources is not high enough to allow the fit of a Sérsic index. Columns (8) and (9) are the circularized effective Sérsic radius, $R^{circ}_{\rm H}$ in kpc, and index, $n^{circ}_{\rm H}$, derived from the Sérsic fit to WFC3 H band images by van der Wel et al. (2012). Column (10) IR surface density in $L_\odot$kpc^{-2}, $\Sigma_{\rm IR} = (L_{\rm IR}/2)/[\pi(R^{circ}_{\rm ALMA})^2]$, where $L_{\rm IR}$ is given in Table 3 and $R^{circ}_{\rm ALMA}$ in Column (6). Column (11) $IR8 = L_{\rm IR}/L_{8\mu m}$ color index. The 8 μm rest-frame luminosities were derived from the observed *Spitzer*-MIPS 24 μm photometry as in Elbaz et al. (2011). $L_{8\mu m}$, hence also $IR8$, can only be determined from the observed 24 μm luminosity for galaxies with $1.5 \leq z \leq 2.5$.

be as large as ∼0.07″, that is, 0.6 kpc. This is the case for GS1, GS3, GS4, and GS8.

We found that these local offsets did not not affect the associations with optical counterparts and that they were smaller than the difference between the positions of the rest-frame UV and FIR light distributions that we discuss in the following sections; except in the case of the galaxy GS4, where the peak of the ALMA emission presented an offset with respect to the HST-WFC3 H-band centroid before applying the local correction for the HST astrometry and fell right on the H-band center after correction.

2.4. Dust, gas, and stellar masses

The ALMA sources were cross-matched with the catalog of GOODS-*Herschel* sources described in Elbaz et al. (2011). All of the sources discussed in the present paper are detected with both *Herschel* photometers PACS and SPIRE with a $S/N > 3$. The 8 GS sources are detected in the two PACS bands and at 250 and 350 μm with SPIRE (including 3 at 500 μm). The 11 UDF sources are detected in the PACS-160 μm and SPIRE-250 μm bands, 9 are detected at 100 μm, 7 at 350 μm, and 2 at 500 μm. The 500 μm is obviously mainly limited by the large beam size at this wavelength with *Herschel* that imposes a hard confusion limit.

The full SEDs including the optical, NIR, MIR, FIR, and sub-millimeter flux densities of the 8 GS galaxies are presented in Fig. 2 together with spectral model fits to the data. The fit of the stellar side of the galaxies was used to determine their photometric redshifts with the EAzY[2] code (Brammer et al. 2008) and stellar masses with the FAST[3] code, which is compatible with EAzY (see the Appendix of Kriek et al. 2009). For the galaxies with spectroscopic redshifts (GS4, GS5, GS6, and GS7), we computed the stellar masses at these spectroscopic values. The case of GS8 is peculiar and is discussed in detail in Sect. 3.1.

For the UDF galaxies, we used the same redshifts as Dunlop et al. (2017) and Rujopakarn et al. (2016) for consistency. We present their dust SEDs in Fig. 3. We computed the stellar masses of the UDF galaxies at those redshifts.

Following Pannella et al. (2015), stellar masses were computed using a delayed exponentially declining star formation history with the Bruzual & Charlot (2003) stellar population synthesis model to fit the observed photometry up to the IRAC 4.5 μm band. We assumed a solar metallicity, a Salpeter (1955) IMF, and a Calzetti et al. (2000) attenuation law with A_V ranging from 0 to 4.

[2] Publicly available at http://www.github.com/gbrammer/eazy-photoz

[3] Publicly available at http://astro.berkeley.edu/~mariska/FAST.html

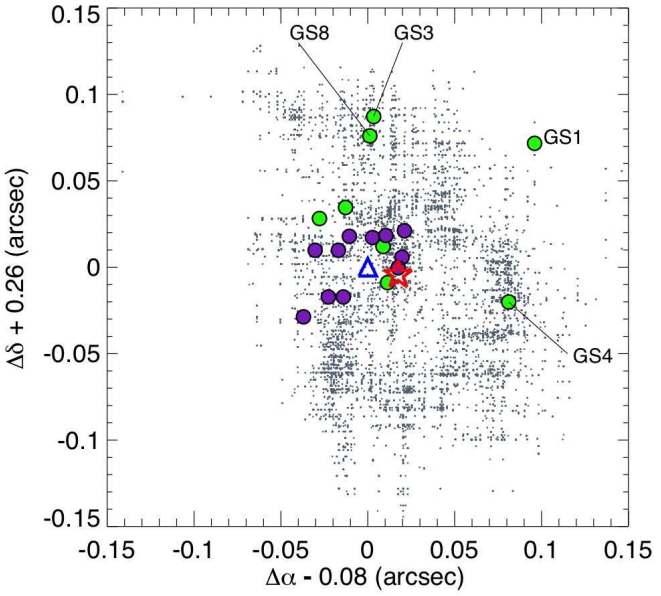

Fig. 1. Astrometric offsets to be applied to the positions of the CANDELS HST catalog in GOODS-*South* to match the positions of the sources detected in Pan-STARRS1 (small gray dots). We centered the diagram on the systematic astrometric correction of [0.08″, −0.26″] introduced by Dunlop et al. (2017) and Rujopakarn et al. (2016) for the HUDF, marked by an open blue triangle. The open red star marks the median of the systematic astrometric correction over the whole 10′ × 15′ GOODS-*South* field [0.095″, −0.264″]. A detailed description of these astrometric offsets will be provided in Dickinson et al. (in prep.). The large green and purple dots mark the 8 GS sources and 11 UDF sources detected with ALMA at 870 μm and 1.3 mm, respectively.

The dust side of the SED of the galaxies (from the *Spitzer* IRS-16 μm and MIPS-24 μm to the ALMA flux densities) was modeled using the IR emission spectra for dust heated by stellar light from Draine & Li (2007) by running the code CIGALE[4] (Noll et al. 2009). Following Draine et al. (2007), we fixed the slope of the distribution of intensities of the interstellar radiation field (ISRF, U), α, to $\alpha = 2$ and adopted an upper limit of $U_{\rm max} = 10^6\ U_\odot$ for the ISRF in units of the solar ISRF.

The best-fitting SED was used to determine the total dust emission, $L_{\rm IR}$, of each galaxy, and a dust mass, $M_{\rm dust}$, listed in Table 3. To derive a gas mass, we determined the total gas-to-dust ratio ($\delta_{\rm GDR} = M_{\rm gas}/M_{\rm dust}$) using Eq. (3) from Leroy et al. (2011) (given in the text of their Sect. 5.2) that links $\delta_{\rm GDR}$ with metallicity for local galaxies, thereby assuming that this relation holds at all redshifts.

$$\log_{10}(\delta_{\rm GDR}) = \log_{10}\left(\frac{M_{HI}+M_{H_2}}{M_{\rm dust}}\right) = (9.4 \pm 1.1) - (0.85 \pm 0.13)\,[12 + \log_{10}(O/H)]\,. \quad (3)$$

Metallicities for our $z \sim 2$ sample of ALMA galaxies were inferred using the mass - metallicity relation described in Eq. (4) taken from Genzel et al. (2012, see their Sect. 2.2) for galaxies at $z = 1.5 - 3$, based on a combination of datasets including the data of Erb et al. (2006).

$$12 + \log_{10}(O/H) = -4.51 + 2.18\ \log_{10}(M_\star/1.7) - 0.0896\,[\log_{10}(M_\star/1.7)]^2. \quad (4)$$

[4] Publicly available at http://cigale.lam.fr.

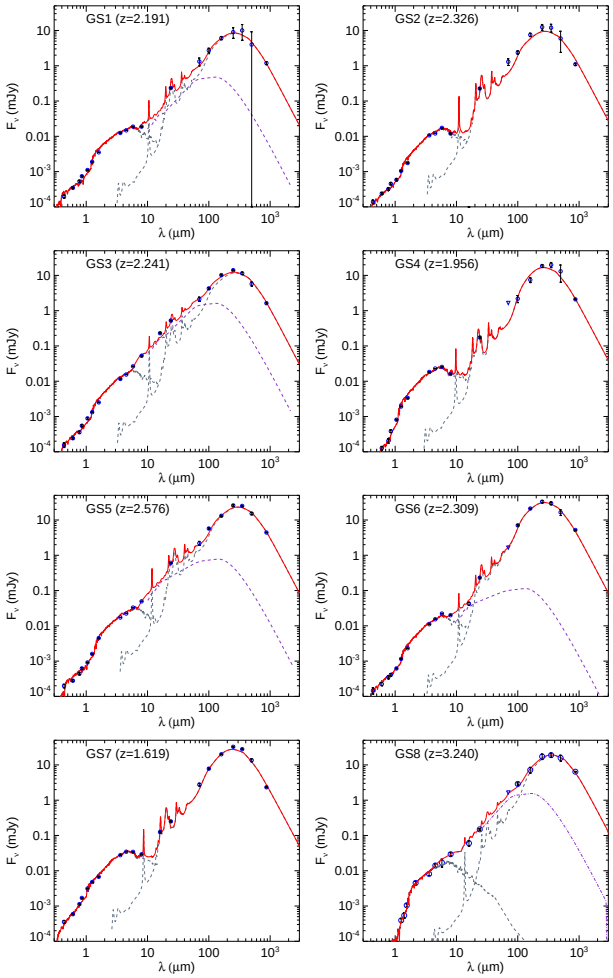

Fig. 2. SEDs of the 8 GS galaxies. The solid red line shows the combination of the model fit of the (i) optical-NIR side of the SEDs done with the FAST code, (ii) IR energy distribution from the best-fitting Draine & Li (2007) model (gray dashed line), and when necessary (iii) the warm dust continuum heated by an AGN using the Mullaney et al. (2011) code "decompIR" (purple dashed line). The specific case of GS8, for which the optical counterpart is nearly undetected, is discussed in Sect. 3.1.

We replaced $M_\star$ in Eq. (4) by $M_\star/1.7$ since Genzel et al. (2012) used a Chabrier IMF whereas here we are using a Salpeter IMF ($M_\star^{\rm Chabrier} = M_\star^{\rm Salpeter}/1.7$). We note a potential caveat in this analysis that is related to the metallicity of dusty starbursts. If the metallicity of starbursts above the MS was found to be systematically higher than the one of galaxies of similar masses within the main sequence (as suggested by Silverman et al. 2015; Puglisi et al. 2017), we would underestimate their gas content and overestimate their depletion time.

Three galaxies are classified as power-law active galactic nuclei (AGN) following the color–color diagram definition of Donley et al. (2012) (blue solid line in Fig. 4): GS3, GS5, and GS8. We used the code "decompIR" by Mullaney et al. (2011) to subtract AGN contributions for all the galaxies. The code decompIR consistently identified an AGN contribution at 8 μm for the three power-law AGNs and at a lower level for the galaxies GS1 and GS6 which stand very close to the limit of Donley et al. (2012) and for which the code decompIR found a small contribution. For all the other galaxies, decompIR did not find any noticeable AGN contribution. The AGN component (shown with the purple dashed line in Fig. 2) was subtracted from the data in a first iteration. We then applied the CIGALE code to fit the

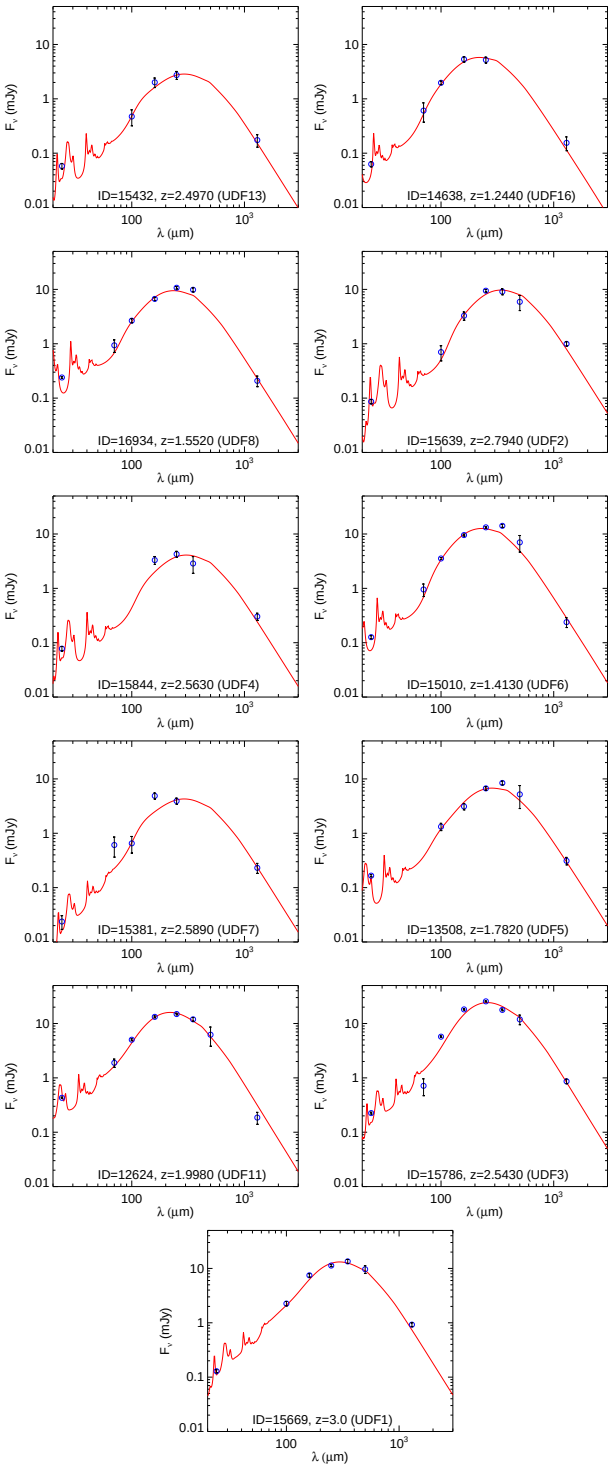

Fig. 3. MIR to sub-millimeter SEDs of the 11 UDF galaxies fitted by the best-fitting IR energy distribution from Draine & Li (2007).

residual emission and determine $L_{\rm IR}$ and $M_{\rm dust}$ free from any AGN contamination. We note, however, that both values are little affected by this AGN emission that mostly contributes to the MIR spectral range.

2.5. Star formation rates and position on the star-formation main sequence

The total SFR of the galaxies is defined as the sum of the IR ($\rm SFR_{IR}$) and uncorrected UV ($\rm SFR_{UV}$) SFR, $\rm SFR_{tot} = SFR_{IR} + SFR_{UV}$. $\rm SFR_{IR}$ and $\rm SFR_{UV}$ were computed following the conversions of Kennicutt (1998) and Daddi et al. (2004) given in Eqs. (5) and (6), where $L_{\rm UV}$ is the rest-frame 1500 Å UV luminosity computed from the best-fitting template obtained with EAzY (uncorrected for attenuation) and $L_{\rm IR}$ is the total dust luminosity given by the best-fitting Draine & Li (2007) model (see Sect. 2.4).

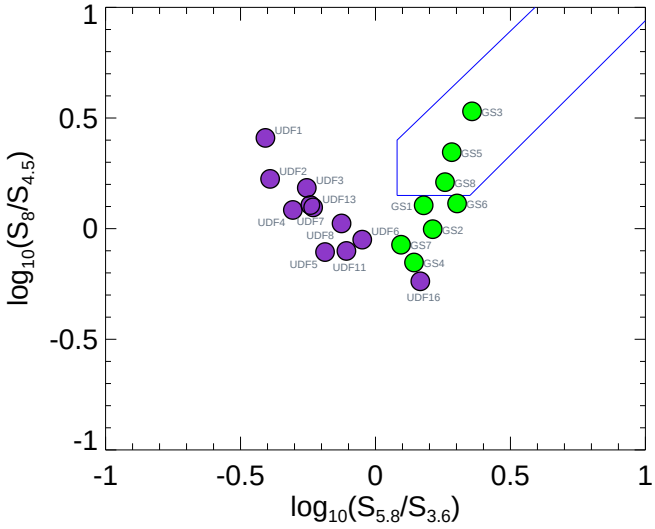

Fig. 4. MIR color–color diagram to search for potential power-law AGNs. Galaxies within the solid blue line are considered as candidate power-law AGNs by Donley et al. (2012).

$$\rm SFR_{IR}\ [M_\odot\ yr^{-1}] = 1.72 \times 10^{-10} \times L_{IR}\ [L_\odot], \quad (5)$$

$$\rm SFR_{UV}\ [M_\odot\ yr^{-1}] = 2.17 \times 10^{-10} \times L_{UV}\ [L_\odot]. \quad (6)$$

We also computed $\rm SFR_{SED}$ by fitting the rest-frame UV-optical-NIR data assuming a constant star formation history and a Calzetti et al. (2000) reddening law (Col. (5) in Table 3). This $\rm SFR_{SED}$ will be compared to $\rm SFR_{tot}$ in order to determine the presence of residual dust attenuation unaccounted for by the *UV*-optical SED fitting. To derive $\rm SFR_{SED}$, we limited ourselves to a constant SFR history in order to avoid the degeneracy between dust attenuation and stellar population ages. Rest-frame magnitudes were computed from the best-fit SED model integrated through the theoretical filters by running EAZY on the multi-wavelength catalog. The resulting $\rm SFR_{tot}$ and $\rm SFR_{SED}$ are listed in Table 3 together with the total IR luminosities obtained from the SED fitting described in Sect. 2.4.

The positions of the ALMA galaxies in the SFR–$M_\star$ plane are shown in Fig. 5 where the eight galaxies from our GOODS-*South* observations are marked with green filled circles. The dashed and two solid black lines show the median and its 68% standard deviation determined by Schreiber et al. (2015). The full catalog of GOODS-*South* galaxies at $1.5 < z < 2.6$ is presented with orange and blue dots for the galaxies with and without a *Herschel* detection, respectively. For the galaxies with no *Herschel* detection, we used $\rm SFR_{SED}$ (blue dots) while for galaxies with a *Herschel* detection, we used $\rm SFR_{tot}$ (orange dots).

The position of the MS, that is, the median of the SFR–$M_\star$ values, varies rapidly with redshift. It increases by a factor 1.9 between $z = 1.5$ and $z = 2.6$ when using the parametrization of the redshift evolution of the MS from Schreiber et al. (2015). In order to place the galaxies at their correct distance relative to the MS in Fig. 5, we first computed this distance at the exact

Table 3. Integrated properties of the ALMA sources.

ID	S	L_{IR}	SFR_{tot}	SFR_{SED}	$\log_{10}(M_\star)$	R_{SB}	$\log_{10}(L_X)$	M^a_{dust}	M^a_{gas}	τ_{dep}
	M	($\times 10^{11} L_\odot$)	($M_\odot$ yr^{-1})	($M_\odot$ yr^{-1})	($M_\odot$)		(erg.s^{-1})	($\times 10^8 M_\odot$)	($\times 10^{10} M_\odot$)	(Myr)
(1)	(2)	(3)	(4)	(5)	(6)	(7)	(8)	(9)	(10)	(11)
GS1	S	17.6 ± 0.9	306 ± 15	107	11.18	1.39	43.44	4.2 ± 0.4	4.9 ± 0.5	161 ± 24
GS2	S	22.2 ± 1.9	385 ± 32	100	11.23	1.47	–	5.1 ± 0.5	6.0 ± 0.6	156 ± 28
GS3	S	25.3 ± 1.3	438 ± 22	112	11.28	1.66	43.44	5.5 ± 0.3	6.3 ± 0.3	144 ± 14
GS4	S	20.9 ± 1.8	360 ± 31	290	11.29	1.70	–	8.2 ± 1.1	9.3 ± 1.3	258 ± 57
GS5	S	66.8 ± 3.3	1154 ± 57	339	11.54	2.41	43.54	14.5 ± 0.7	15.1 ± 0.8	131 ± 13
GS6	M	66.1 ± 3.3	1139 ± 57	107	11.28	4.10	42.29	15.7 ± 1.2	17.9 ± 1.4	158 ± 20
GS7	M	27.9 ± 1.4	482 ± 24	241	10.90	5.36	42.05	10.1 ± 1.2	13.8 ± 1.6	286 ± 48
GS8	U	58.8 ± 3.6	1016 ± 61	567	11.49	1.49	43.26	21.3 ± 4.1	22.4 ± 4.3	220 ± 55
UDF1	U	57.4 ± 2.9	987 ± 49	536	11.03	3.45	43.92	12.6 ± 0.8	16.0 ± 1.0	162 ± 18
UDF2	M	26.0 ± 1.3	448 ± 22	120	11.07	1.71	–	8.3 ± 1.1	10.3 ± 1.4	231 ± 42
UDF3	M	53.4 ± 2.7	928 ± 46	41	10.13	32.61	42.66	11.3 ± 0.6	25.4 ± 1.3	274 ± 27
UDF4	M	10.6 ± 0.6	183 ± 11	48	10.60	2.17	–	2.9 ± 0.3	4.7 ± 0.5	257 ± 43
UDF5	M	7.7 ± 0.4	132 ± 7	127	10.39	3.67	–	4.8 ± 0.8	8.8 ± 1.5	669 ± 147
UDF6	S	9.1 ± 0.5	157 ± 8	–	10.71	2.88	–	4.0 ± 0.6	6.0 ± 0.9	383 ± 76
UDF7	M	11.2 ± 0.6	194 ± 10	95	10.49	2.93	42.68	2.5 ± 0.2	4.4 ± 0.3	224 ± 26
UDF8	S	9.9 ± 0.5	173 ± 9	154	11.12	1.49	43.70	3.2 ± 0.5	3.9 ± 0.6	227 ± 44
UDF11	M	22.5 ± 1.1	396 ± 19	267	10.80	3.99	42.38	4.8 ± 0.2	6.9 ± 0.3	173 ± 17
UDF13	S	7.4 ± 0.5	128 ± 9	166	10.81	0.96	42.45	1.9 ± 0.3	2.7 ± 0.4	214 ± 46
UDF16	S	3.2 ± 0.2	54 ± 3	–	10.80	1.01	–	1.7 ± 0.5	2.4 ± 0.7	439 ± 145

Notes: Column (1) simplified ID. Column (2) visual morphological classification of the rest-frame optical images of the galaxies (from HST-WFC3 H-band): single/isolated galaxy (S), merger (M) and undefined (U). Column (3) total IR (8–1000 μm) luminosity measured from the fit of the data from *Spitzer*, *Herschel*, and ALMA. Column (4) total SFR = SFR_{IR}+SFR_{UV} in $M_\odot$ yr^{-1} where both SFR are defined in Eqs. (5) and (6). Column (5) SFR derived from the fit of the UV-optical-NIR SED in $M_\odot$ yr^{-1} assuming a contant SFR history. Column (6) logarithm of the stellar mass (Salpeter IMF). Column (7) starburstiness, $R_{SB} = SFR/SFR_{MS}$, where SFR_{MS} is the MS SFR at the redshift of the galaxy. Column (8) logarithm of the total 0.5–8 keV X-ray luminosities in erg s^{-1} from Luo et al. (2017). Column (9) dust mass derived from the fit of the FIR SED (see Sect. 2.4). Column (10) gas mass derived from the dust mass in Column (9) following the recipe for the dust-to-gas ratio described in Sect. 2.4. Column (11) depletion time, τ_{dep} ($= M_{gas}/SFR$), in Myr.

redshift of each individual source and then kept this distance but this time relative to the MS at $z = 2$ (dashed line in Fig. 5). As a result, the SFR of a galaxy located at a redshift $z = 1.6$ is shown in Fig. 5 with a higher SFR value equal to its actual SFR multiplied by a factor $SFR_{MS}^{z=2}/SFR_{MS}^{z=1.6}$. This normalization was only used to produce Fig. 5 with realistic galaxy positions in the SFR–$M_\star$ plane.

In the following, we use a single parameter to quantify this distance to the MS called the "starburstiness" as in Elbaz et al. (2011), that is, $R_{SB} = SFR/SFR_{MS}$. Out of the present list of ALMA targets, only 31% (or 15%) may be considered as "starbursts" (SB) defined as galaxies with a starburstiness $R_{SB} > 3$ (or > 4; see Table 3). The remaining 69% (or 85%) consist of galaxies located in the upper part of the MS or slightly above the 68% *rms* of 0.3 dex of the MS. In the following, we refer to MS and SB, which are the star-forming galaxies with $R_{SB} \leq 3$ and >3, respectively, but we study galaxy properties as a function of starburstiness more generally. The postage stamp images of the MS and SB galaxies (HST images with ALMA contours) are shown in Fig. 6 and 7, respectively (except for GS8 discussed in Sect. 3.1 for which the HST and ALMA images correspond to two different galaxies).

3. Results

3.1. Serendipitous detection of an "HST–dark" galaxy at $z \sim 3$

In one out of the eight GS galaxies, GS8, we found an offset between the ALMA and H-band centroids that we attribute to a projection effect, the ALMA source being associated to a background source. The red part of Fig. 8-right showing the H-band contribution to the VIH image shows a clear extension to the North. The offset of 0.35″ between the UV and ALMA centroids is similar to those observed for some of the other galaxies studied here. However, there are three reasons why we believe that the ALMA emission is associated to another galaxy in the case of GS8.

First, there is the above offset of 0.35″ between the H-band and the ALMA centroids, and not only with the UV. Second, the photometric redshift of the foreground galaxy associated with the UV image is $z_{phot} = 1.101$ whereas the FIR SED combining the *Herschel* and ALMA photometric points peaks at 350 μm. If the FIR emission were associated with this galaxy, it would peak at a rest-frame $\lambda = 167$ μm as opposed to the typical galaxies at this redshift which peak around $\lambda = 100\,\mu$m. Third, this galaxy (CANDELS ID = 5893) has an estimated stellar mass of $M_\star = 4.6 \times 10^9$ $M_\odot$. At a $z_{phot} = 1.101$, this galaxy would have an extreme starburstiness of $R_{SB} = 60$ and if the whole FIR emission was to be attributed to this galaxy, it would lead to a dust mass of $M_{dust} = 7.9 \times 10^9$ $M_\odot$, that is, $1.7 \times M_\star$, and a gas mass of $M_{gas} = 2.5 \times 10^{12}$ $M_\odot$. Considering these unrealistic dust temperatures and masses, together with the spatial distribution of the ALMA and H-band light, we believe that the *Herschel* and ALMA emission arise primarily from a background galaxy. Since the foreground galaxy has the CANDELS ID 5893, we decided to call the background galaxy 5893b.

In order to determine the photometric redshift of this galaxy, we modeled the light profile of all the other surrounding galaxies

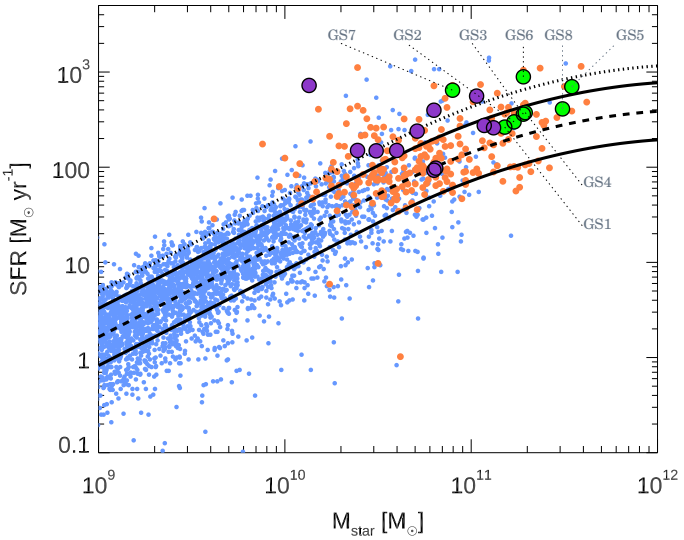

Fig. 5. SFR – $M_\star$ MS at $1.5 < z < 2.5$ as measured in GOODS-*South*. Blue dots: $\mathrm{SFR_{SED}}$ derived from UV-optical-NIR SED fitting. Orange dots: $\mathrm{SFR_{tot}} = \mathrm{SFR_{IR}} + \mathrm{SFR_{UV}}$. In order to keep the relative position of each galaxy with respect to the MS at its redshift, the SFR was multiplied by $\mathrm{SFR^{z}_{MS}/SFR^{z=2}_{MS}}$ using Eq. (9) from Schreiber et al. (2015). The 8 GS and 11 UDF ALMA sources discussed in this paper are shown with green and purple filled symbols, respectively. The $z = 2$ MS and its $rms = 0.3$ dex scatter are shown with a dashed line and solid lines, respectively. The dotted line shows the limit above which galaxies are classified as starbursts ($R_{\mathrm{SB}} = \mathrm{SFR/SFR_{MS}} > 3$).

within an 8″ radius as single Sérsic profiles using `imfit` (Erwin 2015) on the HawK-I Ks-band image (PSF $FWHM = 0.4$ arcsec; Fontana et al. 2014). We then used the results of this modeling to measure the photometry on all the HST images from F435W to F160W, as well as in the *Spitzer* IRAC images from 3.6 to 8 μm. We convolved the Sérsic profiles with the point-spread function of the corresponding image, and only varied the total flux of each galaxy to minimize the χ^2 of the residuals. The resulting photometric measurements for ID5893b are shown in Fig. 9. After this process, ID5893b was only clearly detected in bands J, H from HST–WFC3, Ks from HawK-I, and all the *Spitzer* IRAC bands where it clearly dominates over ID5893.

The photometry obtained for GS8 (ID5893b) was then used to determine a photometric redshift with the program EAZY and a stellar mass with the program FAST. We found $z_{\mathrm{phot}} = 3.24 \pm 0.20$ and $M_\star = 3 \times 10^{11}\ M_\odot$. This photometric redshift is consistent with the observed peak of the FIR SED of ID5893b located at $\lambda_{\mathrm{peak}} \sim 350\,\mu$m.

The resulting starburstiness of GS8, $R_{\mathrm{SB}} = 1.49$, corresponds to a typical MS galaxy at $z \sim 3.24$. The fit of the FIR SED using the Draine and Li model gives a dust mass of $M_{\mathrm{dust}} = 2.3 \times 10^9\ M_\odot$, which is lower than the value estimated for the $z = 1.101$ redshift because the dust mass is very sensitive to the dust temperature, which is much higher here since the peak emission is now located close to 85 μm. The gas fraction, $f_{\mathrm{gas}} = M_{\mathrm{gas}}/(M_{\mathrm{gas}}+M_\star)$, is also reasonable (as opposed to the low-redshift option) since it now reaches a value of 40%.

To conclude, ALMA allowed us to identify a distant counterpart to a previously detected *Herschel* source that was not present in the CANDELS HST catalog (Guo et al. 2013). If one considers the H-band extension that we analyzed above, then GS8 is not, strictly speaking, a HST-dark galaxy, but without ALMA it would have remained HST-dark. We can only extrapolate the implications of this finding on the GS sample of eight galaxies because the UDF galaxies were selected in a blank field that would require an analysis of the existence of HST-dark sources over the whole field. Extrapolating from our small sample, one may expect 10%–15% of the ALMA detections to be associated with an optically dark galaxy. This statement will be studied on a firmer statistical ground in a forthcoming paper discussing a 6.7×10 arcmin^2 extragalactic survey in GOODS-*South* with ALMA at 1.1mm (PI D. Elbaz, Franco et al. in prep.).

3.2. Compact star formation in $z \sim 2$ galaxies

The ALMA images probe the dust continuum emission at typical rest-frame wavelengths of $\lambda^{\mathrm{rest}}_{\mathrm{GS}} = 260\,\mu$m (870 μm observed from $\bar{z}_{\mathrm{GS}} = 2.3$) and $\lambda^{\mathrm{rest}}_{\mathrm{UDF}} = 380\,\mu$m (1.3 mm observed from $\bar{z}_{\mathrm{UDF}} = 2.43$) for the GS and UDF galaxies, respectively. We consider that these two wavelengths to be close enough to probe the same physical origin. We also assume that the median 325 μm wavelength for the whole sample probes the location of the dust heated by the newly formed young stars and that it can therefore, be used to trace the geometry of the star-formation regions.

The first remarkable result that comes out of the resolved dusty star-formation maps obtained with the high-angular-resolution mode of ALMA is their compactness (see Figs. 6 and 7). The optical sizes measured by van der Wel et al. (2012) using a Sérsic profile fitting of the HST-H band images are compared to the ALMA sizes, computed using 2D Gaussian profiles, in Fig. 10. Both are circularized as in Eq. (1). As discussed in Sect. 2.3.2, the Gaussian and Sérsic fits to the ALMA data provide similar sizes.

Over the whole sample of 19 $z \sim 2$ star-forming galaxies resolved with ALMA, we find that the ALMA sizes are systematically smaller than the rest-frame V-band sizes. Similar results have been systematically found by several different authors using galaxy samples selected with different strategies (e.g., Simpson et al. 2015; Hodge et al. 2016; Barro et al. 2016; Rujopakarn et al. 2016; Fujimoto et al. 2017). Using a compilation of ALMA observations with typical angular resolutions of ∼0.6 arcsec (as compared to 0.2 arcsec here), Fujimoto et al. (2017) measured a factor of $R^{circ}_{H}/R^{circ}_{ALMA} \sim 1.4$ (see their Fig. 12) that we have represented with a dashed line in Fig. 10. We can see that most of our galaxies fall within a factor two around this ratio (dotted lines in Fig. 10) except a sub-population of compact sources that we discuss in more detail in the following.

We note however an important caveat related to our sample selection. The condition that we imposed on the GS galaxies resulted in selecting exclusively massive star-forming galaxies with a median $M_\star \sim 1.4 \times 10^{11}\ M_\odot$. The fact that the GS galaxies exhibit systematically smaller sizes than the UDF galaxies may be a consequence of their larger stellar masses if massive galaxies turned out to exhibit particularly compact star-formation distributions. As we show in the following sections, massive galaxies do turn out to exhibit particularly compact star-formation as also found by Barro et al. (2016) and as one would expect if they were candidate progenitors of the population of compact ellipticals at $z \sim 2$ (van der Wel et al. 2014).

As discussed in Sect. 2.3.2 (see also Rujopakarn et al. 2016), the S/N on the UDF ALMA sources in not high enough to provide a robust Sérsic profile fitting and derive a Sérsic index. But for the higher quality of the GS galaxies, we find that the ALMA profiles can be fitted by a Sérsic profile with a median Sérsic index is $n = 1.27 \pm 0.48$, therefore close to an exponential disk. The dusty star-formation regions therefore seem to be disk-like, confirming what was previously found by Hodge et al. (2016).

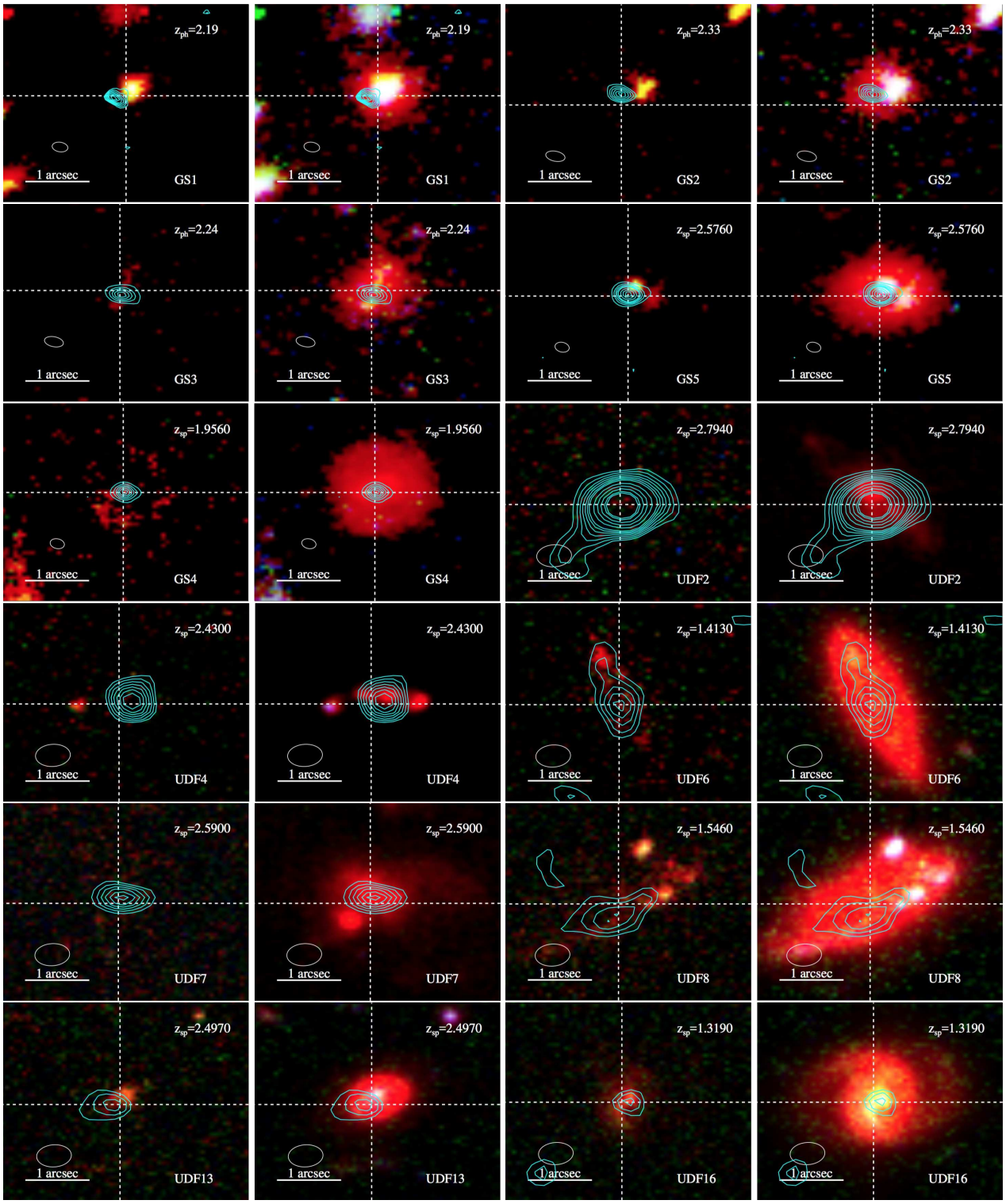

Fig. 6. ALMA contours on HST images for MS galaxies. For each galaxy, the *left column* shows the rest-frame UV from ACS F606W and F814W (equivalent to 2020 and 2710 Å rest-frame at $z \sim 2$), whereas the *right column* includes the HST–WFC3 F160W band (1.6 μm) sampling the rest-frame 5300 Å band at $z \sim 2$ (here RGB = V, I, H). The ALMA contours correspond to 1.3 mm for the UDF sources and 870 μm for the GS source. Contours: for the UDF galaxies increase with steps of 0.5σ starting from 2.2σ, for the GS galaxies: 3σ steps up to 14σ, then 21, 29, 36σ. The dashed crosses are centered on the WFC3 F160W band center. The ALMA PSF is shown in the bottom left of each figure.

3.3. An ALMA view on kpc clumps of star formation

The discovery of giant star-forming regions in the high-redshift population of so-called "chain galaxies" and "clump-cluster galaxies" revealed by the first generation of deep HST images (Cowie et al. 1995; Elmegreen & Elmegreen 2005) started a still-ongoing debate on their role in the stellar mass growth and morphological transformation of galaxies throughout cosmic time. Expected to form as a result of dynamical instabilities in

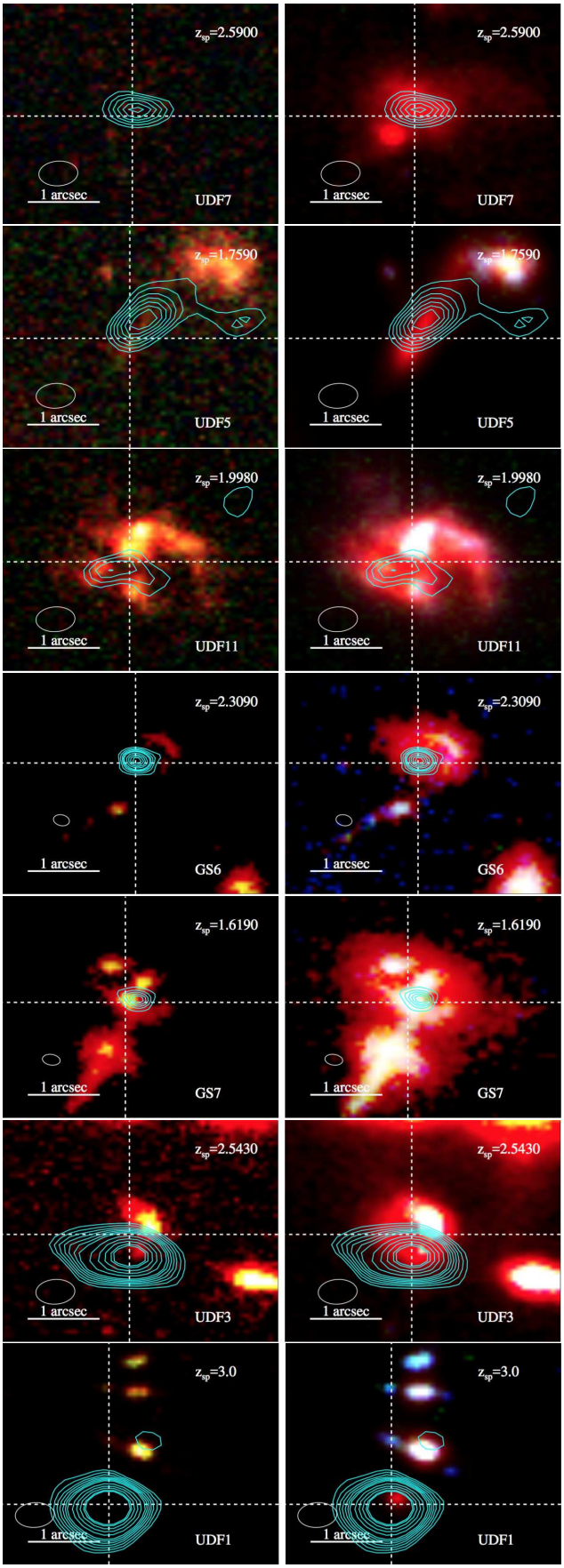

Fig. 7. As in Fig. 6 for the "starburst" galaxies with $R_{SB} > 3$ sorted by increasing R_{SB} *from top to bottom*. Contours as in Fig. 6.

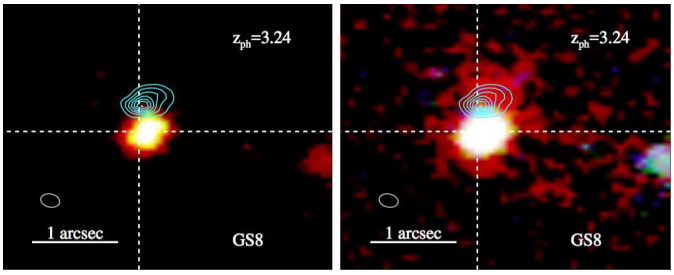

Fig. 8. ALMA contours overlaid on the HST image of the galaxy GS8 (as in Fig. 6).

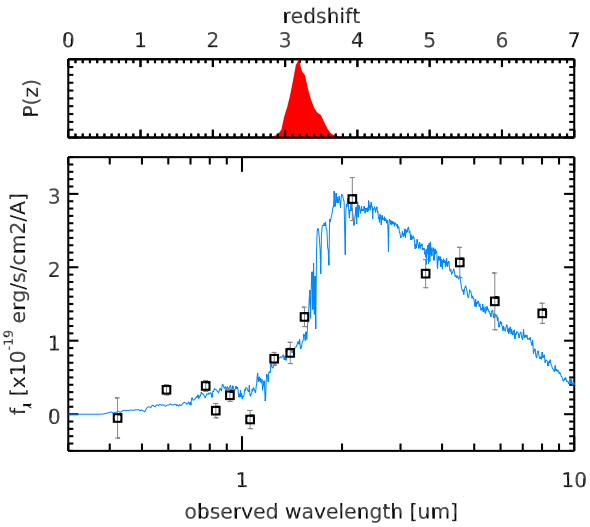

Fig. 9. SED of the offset source GS8 (5893b) measured from aperture photometry at the location of the ALMA source. The photometric redshift probability distribution peaks at $z = 3.24$.

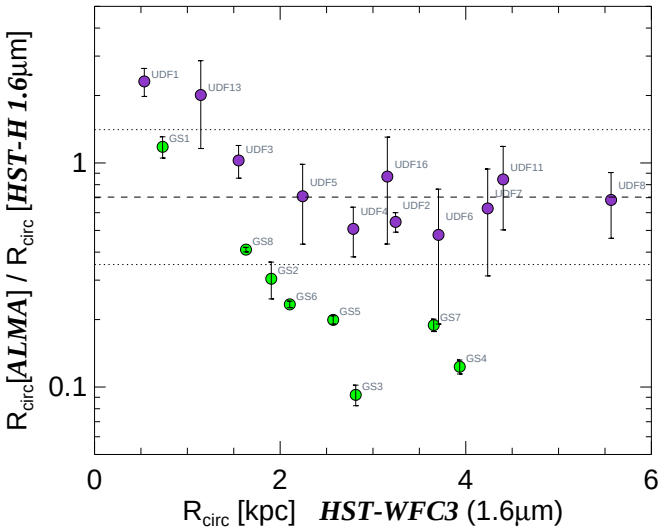

Fig. 10. ALMA circularized effective radii as a function of HST–WFC3 H-band effective radii from van der Wel et al. (2012).

high-redshift gas-rich galaxies, those kpc-size $\sim 10^8$ $M_\odot$ clumps of star formation could lead to the formation of the central bulge of galaxies if they lived long enough to survive their migration from the peripheries to the centers of galaxies (Elmegreen et al. 2008).

The amount of integrated stellar mass growth of a galaxy coming from these kpc clumps remains uncertain. Since $z \sim 2$ galaxies with strong SFR systematically radiate most of their energy from star formation in the FIR/submillimeter, it is only by resolving these galaxies at these long wavelengths that one will be able to determine the role of kiloparsec-size clumps. If clumps of star formation of this size were responsible for a large fraction of the resolved FIR emission of galaxies, this would imply that the physical mechanism responsible for their formation plays an important role in shaping present-day galaxies.

In a recent paper, Hodge et al. (2016) studied the possible existence of kiloparsec-size clumps of star formation with an ALMA follow-up of a sample of 16 $z \sim 2.5$ SMGs with $S_{870\mu m} = 3.4$–9 mJy and $L_{IR} \sim 4 \times 10^{12}$ $L_\odot$. They searched for point-like sources that could be associated with kiloparsec-size clumps using a synthesized beam of $0.17'' \times 0.15''$ *FWHM*, corresponding to a physical size of 1.3 kpc at the median redshift of $z \sim 2.5$ (the analysis was also performed at a resolution of $0.12''$corresponding to 1 kpc). While marginal evidence was found for residual emission that could be associated to the kiloparsec-size clumps, the authors generated some simulated ALMA images of mock galaxies with smooth profiles without any clumps and found that the analysis of the resulting mock ALMA images showed similar signatures of kiloparsec-size clumps with low significance. They therefore concluded that "while there may be a hint of clump-like dust emission in the current 870 μm data on kiloparsec scales, higher S/N observations at higher spatial resolution are required to confirm whether these clumpy structures are indeed real".

Cibinel et al. (2017) used ALMA to spatially resolve the CO(5–4) transition – which probes dense star formation – in the $z = 1.57$ clumpy galaxy UDF6462. In this galaxy, the UV clumps make up between 10% and 40% of the total UV SFR. Using the observed $L'_{CO(5-4)}$–L_{IR} correlation (Daddi et al. 2015), they find that none of the six clumps produces more than 10% of the dusty SFR (upper limit of ~ 5 $M_\odot yr^{-1}$ for a total SFR $= 56$ $M_\odot yr^{-1}$). The limit goes down to less than 18% for the combined contribution of the clumps after stacking all six clumps. If this conclusion may be generalized, it would imply that the giant clumps observed in the UV are not major contributors to the bulk of the stellar mass growth of $z \sim 2$ galaxies.

We designed our ALMA exposures for the eight GS sources (see Sect. 2.3.1) to detect individual clumps of star formation at 870 μm assuming that a clump could be responsible for 20% of the total SFR of a galaxy. In all eight galaxies, we find that the ALMA continuum emission is concentrated in a nuclear region, with no evidence for external clump contributions, similarly to what was found by Cibinel et al. (2017) and Hodge et al. (2016).

Three galaxies among the closest sources of the UDF sample – UDF6, UDF8, and UDF16 at $z_{spec} = 1.413$, 1.546, and 1.319, respectively – present the shape of grand design spirals with a total extent in the rest-frame 6400 Å of ~20–30 kpc (observed WFC3 *H*-band; see bottom right galaxies in Fig. 6). UDF16 is a face-on spiral that shows no evidence for kiloparsec-size UV clumps outside its central UV nucleus whereas UDF6 and UDF8 present clear kiloparsec-size clumps in the rest-frame UV light distribution.

UDF8 presents three clumps in the N-W side and UDF6 one clump in the N-E side. All four UV clumps have a total extent of $0.25''$, that is, 2 kpc at $z \sim 1.5$, giving a radius of about 1 kpc. We note that both galaxies are close to the median SFR of the MS with a starburstiness of $R_{SB} = 1.5$ and 2.9, respectively, and experience a similar SFR ~ 150 $M_\odot$ yr^{-1}. UDF8 presents the largest number of UV clumps; it is the closest galaxy to the median SFR of the MS.

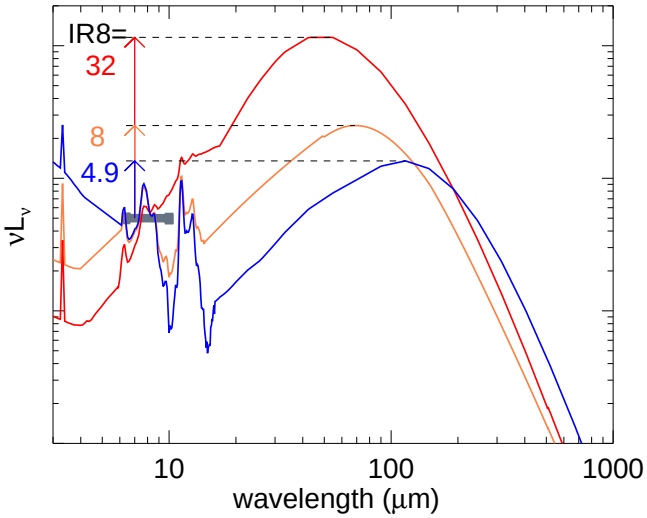

Fig. 11. Three SEDs from the Chary & Elbaz (2001) library normalized to the same $L_{8\mu m}$ (using the IRAC passband centered on 8 μm). We present the SEDs 11, 58, and 95 for which $IR8 = L_{IR}/L_{8\mu m} =$ 4.9, 8, and 32, respectively. The horizontal black solid segment shows the width of the IRAC2 channel centered on 8 μm.

At the typical redshift of $z \sim 1.5$ of these galaxies, the ALMA images of the UDF at 1.3 mm probe the rest-frame 520 μm emission in the rest-frame. This emission is found to peak on the center of the WFC3-*H* band images in both galaxies (crosses in Fig. 6) whereas the UV clumps present a systematic offset. This offset is much larger than the astrometric uncertainty (we note the perfect agreement between ALMA and HST) and the ALMA PSF FWHM (ellipse on the lower-left corner), implying that there is a clear dichotomy in these two galaxies between the young massive stars inhabiting highly attenuated dust clouds and those responsible for the bulk of the UV light. The UV images of UDF6 and UDF8 (left images in Fig. 6) show that no UV light is detected at the location of the peak ALMA emission, which implies that the UV slope is not a good proxy for the amount of dust extinction here.

In both galaxies, the ALMA contours present an extension suggesting some marginal contribution of the kiloparsec-size clumps to the FIR emission. The rest-frame 520 μm contours of UDF6 present a second, less pronounced peak centered on one of the kiloparsec-size clumps and the same is seen, slightly less pronounced, in UDF8 with a contribution from the southern kiloparsec-size clump. However, due to the low S/N of the 1.3 mm images of these sources, this evidence is provided only by the first and second ALMA contours at the 80 and 100 μJy levels, that is, only at the 2σ confidence level. As shown by the simulations of Hodge et al. (2016) discussed above, deeper ALMA integrations would be needed to confirm the detection of the giant clumps in the FIR.

Assuming that the dusty star-formation is indeed not spread in a series of clumps, we consider that it is well characterized by its IR luminosity surface density, Σ_{IR} (Eq. (2)).

3.4. Star-formation compactness and IR8 color index

The IR luminosity density, Σ_{IR} – a proxy for the dusty SFR density – has been found to correlate with an integrated property of local $z \sim 0$ galaxies, the *IR*8 color index (see Fig. 13 of Elbaz et al. 2011). Compact star-forming galaxies were found to exhibit

large values of the $IR8 = L_{\rm IR}/L_{8\mu{\rm m}}$ color index whereas galaxies with extended star formation presented a "normal, universal" $IR8$ ratio of $IR8 \sim 4.9$. Compact and extended star-forming galaxies were distinguished as galaxies with $\Sigma_{\rm IR}$ above and below a critical density of $\Sigma_{\rm IR}^{\rm crit} = 3 \times 10^{10}\ L_\odot\ {\rm kpc}^{-2}$, respectively. In this section, we present a revised version of the local $IR8 - \Sigma_{\rm IR}$ relation and discuss its application to the distant Universe.

The $IR8$ color index measures the ratio of the continuum emission – as measured by the total mid- to far-IR luminosity $L_{\rm IR}$, dominantly due to the emission of big dust grains with a peak emission around $100\,\mu$m – over the emission due to the combination of continuum emission from very small grains (VSGs) of dust and broadband features commonly attributed to polycyclic aromatic hydrocarbons (PAHs; Leger & Puget 1984; Allamandola et al. 1985) – as measured by the $8\,\mu$m *Spitzer*-IRAC broadband filter.

In local galaxies, strong $IR8$ values (red curve in Fig. 11) are systematically associated with compact star formation taking place in merger-driven starbursts. Instead, normal spiral galaxies exhibit strong PAH equivalent widths and a weaker contribution of warm and cold dust continuum in the MIR and FIR (blue curve in Fig. 11). The three template IR SEDs presented in Fig. 11 come from the Chary & Elbaz (2001) library and present $IR8$ values of 4.9, 8, and 32, respectively. Therefore, in local galaxies, $IR8$ not only correlates with star-formation compactness, as probed by $\Sigma_{\rm IR}$, but also with starburstiness, $R_{\rm SB}$ (see Fig. 17 in Elbaz et al. 2011).

In the following, we discuss the physical origin of the $IR8 - \Sigma_{\rm IR}$ relation that may apply to both local and distant galaxies. The interest of this relation is twofold. On one hand, it provides an empirical method to connect integrated and resolved galaxy properties that may be used to derive one from the other. On the other hand, if the relation holds in distant galaxies, $IR8$ and $\Sigma_{\rm IR}$ may both be used to separate compact and extended star formation, and may therefore serve to unveil the role of mergers.

3.4.1. Revised version of the local $IR8 - \Sigma_{\rm IR}$ relation and discussion of its physical origin

To produce their local $IR8 - \Sigma_{\rm IR}$ relation, Elbaz et al. (2011) used IR sizes for local galaxies coming from a combination of radio data (converted to FIR sizes using a correlation observed between FIR and radio sizes) and MIR sizes from *Spitzer*-IRS (from Díaz-Santos et al. 2010).

Here we use sizes directly measured in the FIR coming from a *Herschel*-PACS $70\,\mu$m follow-up of local LIRGs from the Great Observatories All-sky LIRG Survey (GOALS; Armus et al. 2009). Sizes were measured for a total of 293 galaxies including 42 normal galaxies ($10 \le \log(L_{\rm IR}/L_\odot) < 11$), 175 LIRGs ($11 \le \log(L_{\rm IR}/L_\odot) < 12$) and 22 ULIRGs ($12 \le \log(L_{\rm IR}/L_\odot)$). The sizes measured for these galaxies (as described in Díaz-Santos et al. 2017) were used to produce the revised version of the local $IR8 - \Sigma_{\rm IR}$ relation presented in Fig. 12 (top). We also included 11 galaxies with radio sizes (filled squares) and 39 galaxies with MIR sizes from AKARI (filled stars) that were originally used in Elbaz et al. (2011).

This revised $IR8 - \Sigma_{\rm IR}$ relation for local galaxies is amazingly tight with a 68% median absolute deviation (MAD) of only 0.11 dex. The polynomial fit to the sliding median (Eq. (7)) and its MAD are represented by the solid and dashed lines in Fig. 12.

$$\log_{10}(IR8) = (1.02 \pm 0.11) + 0.37 \times \log_{10}\left(\Sigma_{\rm IR}/10^{11}\right) + 0.08 \times \left[\log_{10}\left(\Sigma_{\rm IR}/10^{11}\right)\right]^2. \quad (7)$$

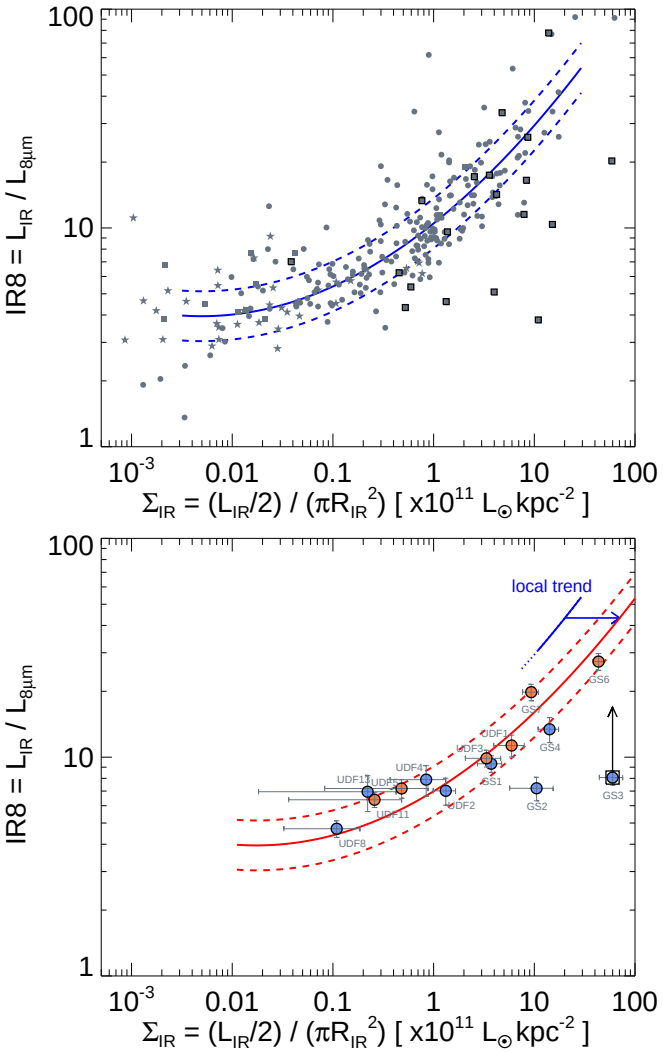

Fig. 12. *Top*: $IR8 - \Sigma_{\rm IR}$ relation for local galaxies. Gray filled dots: 293 galaxies with *Herschel* PACS $70\,\mu$m sizes ($R_{\rm IR} = R_{70\,\mu{\rm m}}$) from Díaz-Santos et al. (2017). Filled squares and stars: 11 and 39 galaxies with radio and MIR sizes from Elbaz et al. (2011). Galaxies with MIR spectral signatures of AGNs (identified by Díaz-Santos et al. 2017) are marked with bold squares. The solid blue line is a polynomial fit to the sliding median described by Eq. (7). The two dashed lines 30% above and below (±0.11 dex) encompass 68% of the galaxies. *Bottom*: position of the $z \sim 2$ ALMA sources on the $IR8 - \Sigma_{\rm IR}$ diagram. The solid and dashed red lines show the local relation shifted to the right by a factor 3.5 to account for the combined effects of the rise of the MS SFR with redshift and decrease of galaxy sizes with redshift. Blue and orange filled dots separate galaxies on or close to the MS ($R_{\rm SB} \le 3$) from starbursts ($R_{\rm SB} > 3$). Only galaxies within $1.5 \le z \le 2.5$ are shown here because of a large and uncertain extrapolation of L_8 from the observed $24\,\mu$m flux density for galaxies outside this redshift range. The black square on GS3 indicates that it is a power-law for which the contribution of the AGN has been corrected in a conservative way.

We find that the trend is relatively flat up to $\Sigma_{\rm IR}^{\rm crit} \sim 3 \times 10^{10}\ L_\odot\ {\rm kpc}^{-2}$ and then rises steeply. Although continuous, this improved relation confirms the existence of two regimes of star formation. Galaxies with extended star formation ($\Sigma_{\rm IR} < 3 \times 10^{10}\ L_\odot\ {\rm kpc}^{-2}$) have $IR8 = 4$–5, whereas compact star-forming galaxies reach $IR8$ values well above 10.

We wish to emphasize that most of the outliers below the relation are galaxies identified as power-law AGNs by Díaz-Santos et al. (2017) from their MIR spectra (thick black

squares in Fig. 12, top). This trend may either be explained by (i) a contribution to the 8 μm emission by warm dust heated by AGN, and/or (ii) a physical connection between star-formation compactness and AGN activity.

The physical origin of this tight correlation can now be better understood thanks to the analysis of Díaz-Santos et al. (2017) who present a similarly tight relation between $L_{\rm IR}/L_{[\rm CII]158\,\mu m}$ and $\Sigma_{\rm IR}$. The [CII]158 μm emission comes from the same region as the PAHs that contribute to the 8 μm luminosity, namely the PDR or photo-dissociation region. In both cases, there is a nearly flat $IR8$ and $L_{\rm IR}/L_{[\rm CII]158\,\mu m}$ ratio with increasing $\Sigma_{\rm IR}$ up to the same critical density, $\Sigma_{\rm IR}^{\rm crit} \sim 3$–$5\times10^{10}$ $L_\odot$ kpc^{-2} (see their Fig. 2 (middle right), which shows $L_{[\rm CII]158\,\mu m}/L_{\rm IR}$, analogous to $1/IR8$ here). Further, $IR8$ and the $L_{\rm IR}/L_{[\rm CII]158\,\mu m}$ ratio both increase with increasing $\Sigma_{\rm IR}$. This behavior may be understood with the concept of "dust-bounded" star-formation nebulae described in Abel et al. (2009). The idea proposed in this paper and discussed in Díaz-Santos et al. (2017) involves the role of dust that absorbs part of the ionizing radiation and therefore prevents it from reaching the PDR region. This leads to a rise of the dust temperature and consequently also of the total IR luminosity emitted, proportional to $T_{\rm dust}^{4+\beta}$ (where β is the emissivity of the dust), and a drop of the emission in [CII] and PAHs from the PDR. In the local Universe, merger-driven starbursts are systematically associated with such young and compact star-formation regions that may be considered as dust-bounded, with the consequence that $IR8$ and $L_{\rm IR}/L_{[\rm CII]158\,\mu m}$ rise during the merger-driven starburst. Díaz-Santos et al. (2017) find that the ratio of the intensity of the interstellar radiation field, G, over the average PDR hydrogen density, $n_{\rm H}$, $G/n_{\rm H}$, remains constant below $\Sigma_{\rm IR}^{\rm crit}$ and increases rapidly with $\Sigma_{\rm IR}$ above $\Sigma_{\rm IR}^{\rm crit}$.

3.4.2. The $IR8 - \Sigma_{\rm IR}$ relation for $z \sim 2$ ALMA galaxies

The positions of the $z \sim 2$ ALMA galaxies in the $IR8 - \Sigma_{\rm IR}$ plan are shown in Fig. 12 (bottom). $IR8$ values were only computed for galaxies with $1.5 \leq z \leq 2.5$ in order to include the dominant 7.7 μm PAH feature in the observed *Spitzer*-MIPS 24 μm passband. The power-law AGN GS3 (see Fig. 4, GS5 and GS8 are out of the redshift range where $IR8$ can be computed) is marked with a bold square and an upward pointing arrow. This arrow illustrates the fact that the AGN contribution to the rest-frame 8 μm luminosity is uncertain. Our estimate of L_8 was done assuming a conservative SED for the star-formation component. This assumption does not affect the determination of $L_{\rm IR}$ but does affect L_8. We found that using an SED like Arp 220, for example, would nearly equally well fit the IR SED if the AGN produced the bulk of L_8. In this case, $IR8$ would be increased by a large factor, potentially bringing the galaxy in the relation followed by the rest of the sample.

First, we note that the $z \sim 2$ sample follows a correlation like the local galaxies. Second, one can see that galaxies on and above the MS are not separated as is the case for local galaxies where "starbursts" present a compact geometry with $\Sigma_{\rm IR}^{\rm crit} > \Sigma_{\rm IR}^{\rm crit}$ while MS galaxies experience more extended star formation. Galaxies three times above the MS (i.e., with $R_{\rm SB} > 3$) are marked with orange symbols in Fig. 12 (bottom), while MS galaxies below this $R_{\rm SB}$ value are represented with blue symbols. Both types span the full dynamic range in $\Sigma_{\rm IR}$. However, as we see in the following, it is possible that some of our MS are actually experiencing a merger that enhances their star formation by a moderate factor.

In the framework of the dust-bounded star-formation regions interpretation that we discussed above, galaxies with a larger $IR8$ are observed in a younger stage, that precedes the destruction of the dust within the HII region. However, the typical $\Sigma_{\rm IR}$ of a galaxy at the median redshift of $z \sim 2.3$ of our sample was larger than that of a local galaxy. We estimate this factor to be around $\sim$3.5 as a result of the fact that the SFR of MS galaxies was 20 times greater (Schreiber et al. 2015) and the typical size of a star-forming galaxy was $(1+z)^{0.75}$ times smaller (van der Wel et al. 2012). We find that the red solid and dashed lines that represent the local $IR8 - \Sigma_{\rm IR}$ relation shifted by this factor 3.5 do provide a good fit to the ALMA data. This suggests that $IR8$ may serve as a good proxy for $\Sigma_{\rm IR}$ even in the distant Universe.

We note that the fact that high-redshift galaxies are more metal-poor than present-day galaxies, they may naturally exhibit weaker PAH emission, and therefore stronger $IR8$ values, as discussed in Shivaei et al. (2017). However, star-formation in high-z galaxies is taking place both in more compact regions and in less metal-rich environments, and disentangling both effects might be quite complex (see Schreiber et al. 2017).

3.5. Star-formation compactness and AGN activity

Out of our sample of 19 ALMA galaxies, 11 are detected in *X-rays* with the 7-Msec exposure of the *Chandra* Deep Field-*South* image (Luo et al. 2017). Following the commonly used AGN definition (also used in Luo et al. 2017), we classify an X-ray source as an AGN when its total X-ray luminosity integrated over the whole 0.5–7 keV range satisfies $L_X \geq 10^{42.5}$ erg s^{-1}. With this AGN definition, we detect a total of eight AGNs. The three power-law AGNs (see Fig. 4) are all identified as X-ray AGNs with $L_X \geq 10^{43}$ erg s^{-1}.

We find that the proportion of galaxies hosting an AGNs rises with increasing $\Sigma_{\rm IR}$: 75% of the galaxies with $\Sigma_{\rm IR} \geq 3\times10^{11}$ $L_\odot$ kpc^{-2} harbor an AGN (6 out of 8 galaxies). Hence there is a clear increase of the fraction of AGNs among the galaxies with compact star formation within the limited statistics of the present sample. This suggests that the physical mechanism responsible for the rise in star-formation compactness also efficiently feeds the central black hole. Such a relationship was also found by Chang et al. (2017a,b).

We also note that only 25% of the AGNs are associated with galaxies the we visually classified as morphologically disturbed, that is, mergers. The rest of the AGN population is morphologically classified as either isolated or unknown. Interestingly, the AGN fraction exhibits a tighter link with the FIR luminosity density, and therefore, with the star-formation compactness, than with the visual identification of a merger signature. However, we cannot rule out the possibility that these galaxies are in the late stage of a merger, which at these redshifts would not present clearly identifiable morphological perturbations. We discuss in Sect. 4.4 the possibility that some of the MS galaxies may be in such a late-stage merger phase.

4. Starbursts in and out of the star-formation main sequence

4.1. Gas fraction and depletion time of galaxies in and out of the star-formation main sequence

Our sample of galaxies presents some systematic biases that need to be carefully taken into account before discussing its ALMA

properties. In order to dominantly include normal MS galaxies, our *Herschel* selected sample of eight GS galaxies is heavily biased towards massive galaxies. As a result, our discussion on $z \sim 2$ MS galaxies is limited to a stellar mass of $M_\star > 10^{11}\ M_\odot$. Only three galaxies of the HUDF sample fall in the same mass range.

The characteristic mass of the MS galaxies discussed here is $M_\star = 1.4 \times 10^{11} M_\odot$, as compared to $M_\star = 5 \times 10^{10} M_\odot$ for starbursts. However, despite this mass segregation, we do find that both our MS and starburst galaxies follow the global trends observed using a much wider sample of nearly 1300 galaxies (combining individual detections and stacks, Tacconi et al. 2018; see Fig. 13) as well as the original relation of Magdis et al. (2012a; purple line in Fig. 13 (top), observed only up to $R_{\rm SB} = 3$, extrapolated above this value). We observe a similar rise of the gas fraction and SFE (hence a drop in depletion time) as the global trends for galaxies with the median properties of our sample ($M_\star = 1.4 \times 10^{11} M_\odot$, $z = 2.3$) summarized in Eq. (8) and Eq. (9) (derived from the Table 3 of Tacconi et al. 2018).

$$\sigma_{\rm gas} = \frac{M_{\rm gas}}{M_\star} = \left[0.59^{+0.37}_{-0.24}\right] \times R_{\rm SB}^{0.53}, \quad (8)$$

$$\tau_{\rm dep} = \frac{M_{\rm gas}}{\rm SFR} = \left[300^{+63}_{-52}\right] \times R_{\rm SB}^{-0.44} \ \ [\rm Myr]. \quad (9)$$

We note that these trends only weakly depend on stellar mass. The typical depletion time for a MS galaxy at this mass and redshift is 300 Myr (for a Salpeter IMF and 660 Myr for a Chabrier IMF as used in Tacconi et al. 2018). The agreement with the global trends apply both for our MS galaxies (cyan filled dots) and starbursts (orange filled dots). We can clearly see that even though our sample has a strong mass selection, it does follow very well the trend found by a sample spanning a wider dynamic range of stellar masses. Galaxies more massive than $M_\star = 10^{11}\ M_\odot$ (surrounded with an empty circle in Fig. 13) do not depart from these global trends. We note however the presence of four MS galaxies with depletion times that are typical of starbursts (~150 Myr, labeled in red in Fig. 13). Section 4.4 is dedicated to these galaxies.

After a rapid analysis of the distribution of the galaxies in Fig. 13 (bottom), one may conclude that starbursts do not form stars more efficiently than MS galaxies. Instead, it is our sample selection that revealed these four exceptional MS galaxies with star formation efficiencies comparable to those of starbursts. A selection that combines the requirement of *Herschel* detections and high stellar masses. Globally, the two Fig. 13 show that our sample is fully consistent with the fact that starbursts both exhibit higher gas fractions and shorter depletion times.

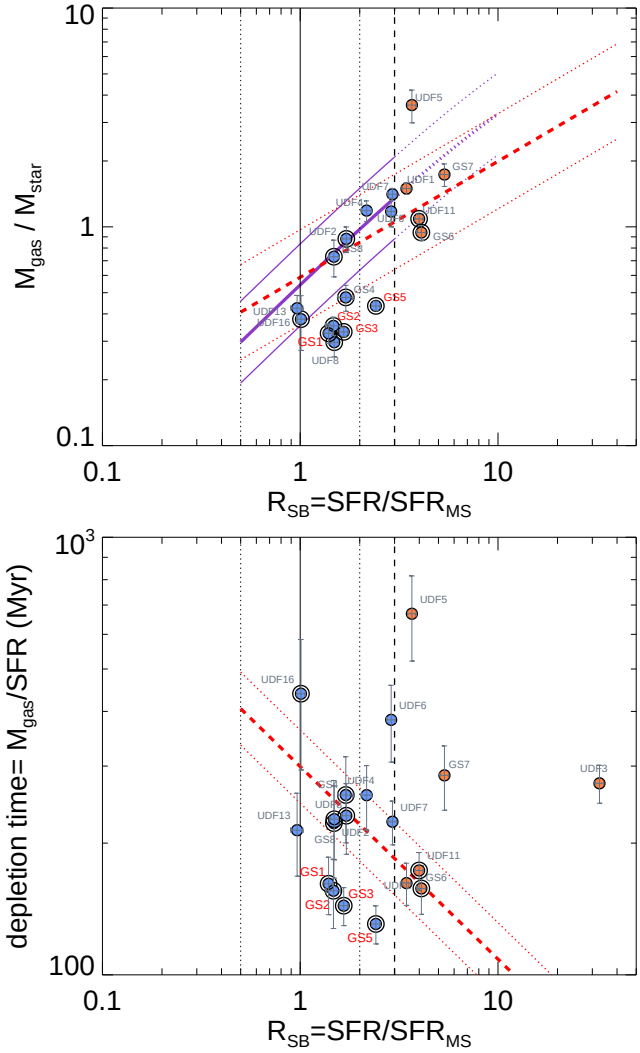

Fig. 13. Gas fraction (*top*) and depletion time (*bottom*) as a function of starburstiness, $R_{\rm SB}$ = SFR/SFR$_{\rm MS}$. The MS and its 68% scatter are shown with a solid and dotted lines, respectively. MS galaxies ($R_{\rm SB} \leq 3$, left of vertical dashed line) are marked with cyan filled dots; starbursts above the MS (i.e., $R_{\rm SB} > 3$) with orange filled dots. Galaxies with $M_\star > 10^{11}\ M_\odot$ are surrounded with an open circle. The dashed and dotted red lines show the relations and their scatter obtained by Tacconi et al. (2018) for the median $z = 2.3$ and $M_\star^{\rm Salpeter} = 1.4 \times 10^{11} M_\odot$ of this galaxy sample (see Eqs. (8) and (9)). The solid purple line in the top figure shows the relation obtained by Magdis et al. (2012a) scaled to the median stellar mass of the sample. The four galaxies with red labels (GS1, GS2, GS3, GS5) present short depletion times typical of starbursts (they are discussed in Sect. 4.4).

4.2. Starbursts above the main sequence

We visually classified galaxies from the HST H-band images, that is, visible in the rest-frame, in two broad categories: single/isolated galaxy (S), with no clear sign of perturbation, and galaxies with a perturbed morphology that we listed as mergers (M) in Table 3. Two cases are listed as undefined: GS8, discussed in detail in Sect. 3.1, and UDF1, which appears point-like even in the HST image.

We find that all the starbursts of our sample (here defined as galaxies with $R_{\rm SB} > 3$) exhibit the morphologies of mergers (see Fig. 7). Instead, the median starburstiness of the single/isolated galaxies (S-type) is $R_{\rm SB} \sim 1.5$, that is, nearly equal to the median of the MS. As noted in Sect. 4.1, star formation in starbursts is not only associated with a shorter depletion time but also with an enhanced gas fraction (see Fig. 13). This increase of the gas fraction during a merger event could be due to the impact of the merger on the circum-galactic gas surrounding the galaxies before the merger. This gas may be driven towards the center of the galaxies. To our knowledge, hydrodynamic simulations accounting for the presence of circum-galactic matter, and its possible infall induced during a merger, do not exist at present. Such simulations should be performed to test this hypothesis.

We searched for a signature in the IR luminosity surface density, but we did not find any trend, neither with starburstiness (Fig. 14) or gas fraction (Fig. 15). We describe below how we determined the characteristic IR luminosity surface density of a MS at this mass and redshift. The SFR of a MS galaxy at our

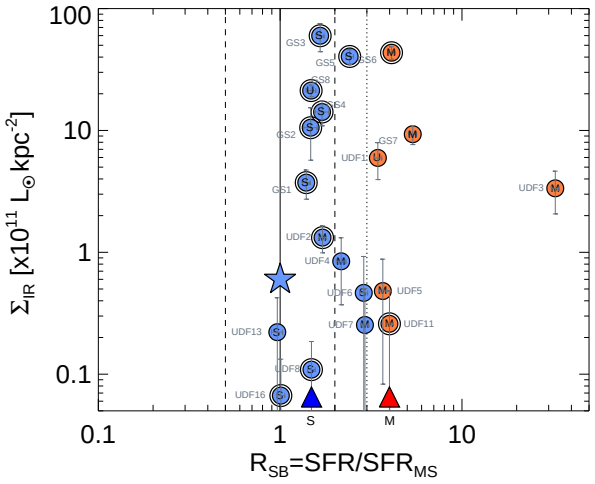

Fig. 14. IR luminosity surface density, Σ_{IR}, as a function of starburstiness, R_{SB}. Blue and orange filled dots separate galaxies on and three times above the MS. The letters indicate the morphology. The median position of mergers (M) and "single/isolated" (S) galaxies are indicated at the bottom with a red triangle and a blue triangle, respectively. The blue star shows the position of typical $z \sim 2$ MS galaxies. The most massive galaxies ($M_\star > 10^{11}$ $M_\odot$) are surrounded with an open circle.

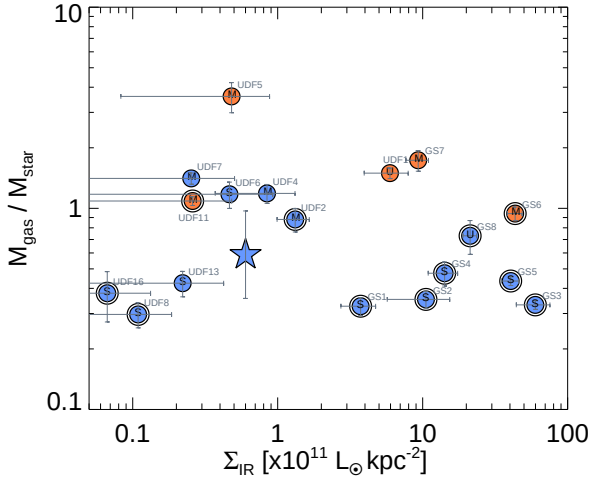

Fig. 15. Gas fraction (in %) as a function of IR luminosity surface density, Σ_{IR}. Caption as in Fig. 14.

median redshift of $z = 2.3$ and stellar mass of $M_\star = 1.4 \times 10^{11}$ $M_\odot$ is $\mathrm{SFR}^{MS} = 224$ $M_\odot$ yr^{-1} (from Schreiber et al. 2015), which corresponds to $L_{IR}^{MS} = 1.3 \times 10^{12}$ $L_\odot$ using the Kennicutt (1998) relation for a Salpeter IMF. The typical H-band size of such galaxy is given by the relation shown in Fig. 5 of Tadaki et al. (2017): $\log_{10}[R_e^{MS}(H)] = 0.14 \times \log_{10}[M_\star^{Salpeter}/1.7]$–1.11, that is, 2.6 kpc. We used the tyical $R_e^{MS}(H)/R_e^{MS}(870\,\mu m) = 1.4$ ratio from Fujimoto et al. (2017) to derive a characteristic ALMA size of $R_e^{MS}(870\,\mu m) = 1.85$ kpc. The resulting characteristic IR luminosity surface density is $\Sigma_{IR} = 6 \times 10^{10}$ $L_\odot$ kpc^{-2}.

4.3. Spatial offset between UV and FIR light distributions

We can see in Fig. 7 that there is a systematic offset between the UV and ALMA light distributions in starbursts three times above the main sequence. Such spatial separation was already noted in the literature (see Rujopakarn et al. 2016; Barro et al. 2016; Hodge et al. 2016). This suggests that the use of the UV emission to determine the total SFR of starburst galaxies may lead to strong underestimates, even when accounting for a dust attenuation correction based on the UV slope. We show that this is indeed the case in Fig. 16.

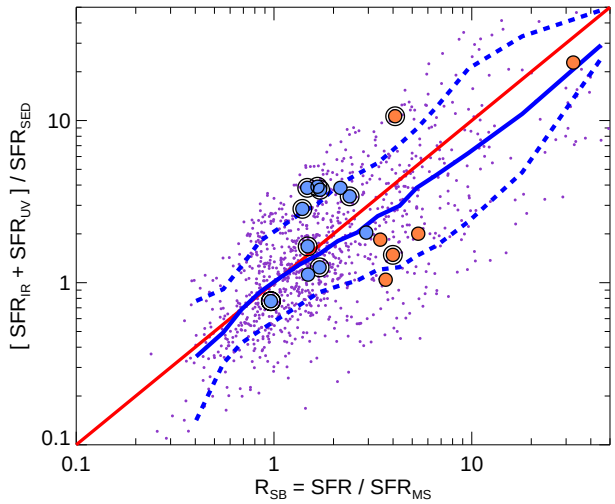

Fig. 16. Excess of total SFR, $\mathrm{SFR_{tot}} = \mathrm{SFR_{IR}} + \mathrm{SFR_{UV}}$, with respect to the $\mathrm{SFR_{SED}}$ determined by fitting the rest-frame UV-optical-NIR, as a function of starburstiness, $R_{SB} = \mathrm{SFR_{tot}/SFR_{MS}}$. The purple dots show the positions of the galaxies from all four CANDELS fields with an *Herschel* detection with $1.5 \leq z \leq 2.5$. Sliding median of the purple points in thick solid blue line and 68% median absolute deviation in dashed. Symbols for the ALMA galaxies as in Fig. 13. The red line marks the direct proportionality. The solid and dashed blue lines indicate the sliding median and its 68% absolute deviation.

The rest-frame far-UV emission of $z \sim 2$ galaxies is commonly used to derive total SFR after applying a correction for dust attenuation either from the determination of the UV-slope, β, or from the modeling of the full UV-optical SED with, for example, the Calzetti et al. (2000) attenuation law (see e.g., Meurer et al. 1999; Calzetti et al. 2000; Daddi et al. 2004; Overzier et al. 2011; Buat et al. 2012; Reddy et al. 2012, Heinis et al. 2013; Pannella et al. 2015). The average consistency for most galaxies between both ways to derive total SFR – (1) $\mathrm{SFR_{tot}} = \mathrm{SFR_{IR}} + \mathrm{SFR_{UV}}$ and (2) $\mathrm{SFR_{tot}} = \mathrm{SFR_{SED}}$ or $\mathrm{SFR_{UV}^{corrected}}$ – suggests that the young massive stars responsible for the UV and FIR emission are located in the same region. Alternatively, this consistency would be difficult to explain if a spatial segregation was found for most galaxies.

To address this question, we compare the ratio of both estimates of the total SFR, $[\mathrm{SFR_{IR}} + \mathrm{SFR_{UV}}]/\mathrm{SFR_{SED}}$, to the distance to the MS, $R_{SB} = \mathrm{SFR/SFR_{MS}}$. The purple dots in Fig. 16 show the positions of all the galaxies with $1.5 \leq z \leq 2.5$ detected in at least one *Herschel* band (to ensure a robust determination of L_{IR}) in all four CANDELS fields (GOODS-S, GOODS-N, UDS, and CANDELS-COSMOS) and in the COSMOS 2 degree field. The sliding median (thick solid blue line, and 68% dispersion in dashed) shows that $\mathrm{SFR_{SED}}$ and $[\mathrm{SFR_{IR}} + \mathrm{SFR_{UV}}]$ provide the same estimate of $\mathrm{SFR_{tot}}$ within 0.3 dex for MS galaxies, that is, where $R_{SB} \sim 1$. We note that the density of the purple points at the [1,1] position is not representative of the actual number of MS galaxies because at the *Herschel* sensitivity limit, only the most massive MS galaxies are detected. Therefore this result is consistent with previous studies which found that, on average, both SFR estimators are consistent for typical MS galaxies.

However, the sliding median of the relation between $[\mathrm{SFR_{IR}} + \mathrm{SFR_{UV}}]/\mathrm{SFR_{SED}}$ and R_{SB} (solid blue line) nearly follows

the line of direct proportionality (solid red line). The resolved ALMA images offer a nice explanation for this increasing "incorrectness" of SFR_{SED} with increasing "starburstiness" by showing a clear offset between the UV and IR light distributions in starbursts (Fig. 7). A galaxy with $R_{SB} \sim 4$ forms stars with an intensity that is typically four times greater than the one derived from SED fitting. This implies that galaxies experiencing a starburst phase may be incorrectly interpreted as normal MS star-forming galaxies in the absence of direct FIR measurements. Equivalently, R_{SB} is a good proxy for the incorrectness of SED-derived SFR. This is particularly true in the cases of GS6 and UDF3, for which SFR_{SED} is incorrect by a factor 11 and 23, respectively (the two highest ALMA points in Fig. 16).

Among the ALMA galaxies that belong to the MS (blue symbols in Fig. 16), a group of galaxies cluster around $[SFR_{IR}+SFR_{UV}]/SFR_{SED} \sim 1$ as expected for typical MS galaxies. Their three color V,I,H images (from the third to last row of Fig. 6 except UDF2 and UDF4) show that these galaxies present large disk shapes with no obvious sign of disturbance and no strong offset between the UV and IR light. Here the UV and FIR light come from the same region, consistent with the fact that $[SFR_{IR}+SFR_{UV}]$ and SFR_{SED} are in good agreement, although with a slight offset for UDF13.

However, our sample also includes a group of MS galaxies with a strong excess of heavily obscured star formation with $[SFR_{IR}+SFR_{UV}]/SFR_{SED} \sim 4$. This group includes the four galaxies GS1, GS2, GS3, and GS5 marked with red labels in Fig. 13 (the first four images in Fig. 6) and discussed in Sect. 4.4, as well as UDF2 and UDF4. SED-fitting systematically underestimates the amount of dust-attenuated star formation in these MS galaxies with an amount that is equivalent to starbursts with a SFR typically five times above the MS, even though they lie on the MS.

4.4. Compact starbursts hidden within the main sequence

The depletion time, τ_{dep}, of our galaxy sample decreases with IR luminosity surface density following Eq. (10) (Fig. 17).

$$\tau_{dep} = [276^{+85}_{-87}] \times \Sigma_{IR}^{-0.16}. \quad (10)$$

This implies that the galaxies hosting the most compact star formation convert their gas reservoirs in stars more efficiently. The six galaxies forming stars with the shortest depletion times ($\tau_{dep} \sim 146$ Myr) present a $\Sigma_{IR} = 1.5 \times 10^{12}\ L_\odot\ kpc^{-2}$, or equivalently 255 $M_\odot\ yr^{-1}\ kpc^{-2}$. Interestingly, four out of these six galaxies are MS galaxies, those that we marked with red labels in Fig. 13 (GS1, GS2, GS3, and GS5). In comparison, the typical depletion time for a MS galaxy of similar mass and redshift is more than twice longer (blue star in Fig. 17) and its IR luminosity density is 25 times lower, $\Sigma_{IR}^{MS} = 6 \times 10^{10}\ L_\odot\ kpc^{-2}$.

These four MS galaxies exhibit (i) low gas fractions, (ii) short depletion times, and (iii) extreme IR luminosity surface densities. They present all the characteristics of starbursts despite their location within the standard deviation of the MS, and therefore can be seen as compact starburst hidden within the MS.

We checked whether these galaxies could be mistakenly identified as part of the MS while being in reality starbursts. Only one of them, GS5, has a spectroscopic redshift, whereas the other three only have photometric redshifts. In order to determine how the uncertainty on the redshifts of these galaxies may impact their starburstiness, we looked at the 16 and 84 percentile values of these redshifts from their probability distribution functions. All three have very accurately determined photometric

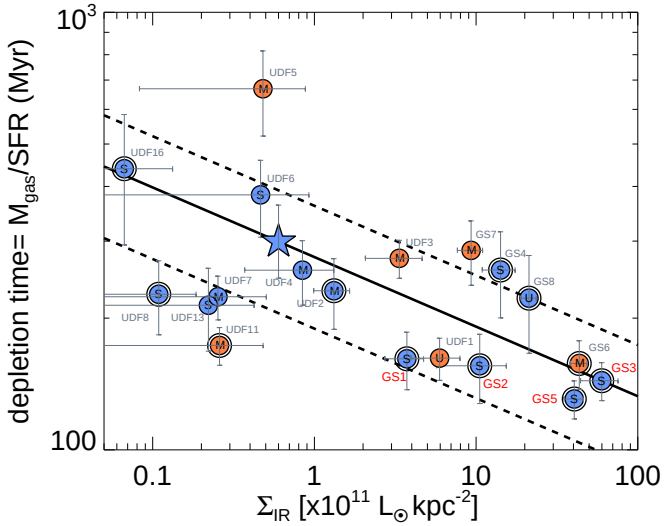

Fig. 17. Depletion time as a function IR luminosity surface density, Σ_{IR}. The blue star shows the typical depletion time of $z \sim 2.3$ MS galaxies. Colors and symbols as in Fig. 14. The four MS galaxies with the shortest depletion times are identified with red labels (GS1, GS2, GS3, and GS5) as in Fig. 13. The solid and dashed lines are the fit to the sliding median and its 68% scatter.

redshifts with $\delta z/(1+z)$ values of $[-1.9,+0.9]$, $[-19,+22]$, and $[-1.3,+1.1] \times 10^{-3}$ for GS1, GS2, and GS3, respectively. If we combine these redshift uncertainties with the error bars on the photometric measurements, we find that the resulting stellar masses vary by ±11%, 1% and 2%, respectively. This would not modify their positions relative to the MS. A more important potential caveat comes from the possible contribution of an AGN component to the photometry. We discussed the contribution of AGNs to the multi-wavelength SEDs in Sect. 2.4 but limiting ourselves to their impact on the IR luminosity and dust mass. However, AGNs may also contaminate the rest-frame NIR emission of the galaxies whose stellar masses may then be overestimated if the AGN contribution is thought to be due to stellar emission. To our knowledge, however, there is no reliable way to cleanly extrapolate the SED of the dusty AGN component to the NIR and optical range. In the absence of robust model or template AGN SEDs that would allow such extrapolation, we have decided to quantify this effect by re-computing the stellar masses of GS1, GS3, and GS5 – where we found evidence for the presence of dust heated by an AGN – after excluding the NIR photometry coming from IRAC, which would be the wavelength the most contaminated by hot dust from an AGN. The new stellar masses are the same for GS3, 2% higher for GS1, and 65% lower for GS5. GS5 that had a starburstiness of $R_{SB} = 2.4$ when using the full SED to determine its stellar mass, would have a revised value of $R_{SB} = 4$ that would make it a starburst under our definition of $R_{SB} > 3$ for starbursts. In conclusion, we find that the bulk of these compact starbursts hidden in the MS would remain MS galaxies even when including potential uncertainties on their redshift and AGN contamination with the exception of GS5 that may well be a starburst if an AGN does indeed generate the bulk of its NIR emission.

A third common point between these galaxies is particularly striking: they all exhibit a strong dichotomy between their IR and UV light distributions (see Fig. 6). This offset explains why SFR_{SED} is a poor proxy for $SFR_{IR}+SFR_{UV}$ for these galaxies. Therefore, these MS galaxies present equivalent offsets and SFR_{SED} "incorrectness" to the "starburst" galaxies lying above

the MS, but they belong to the MS itself. Nevertheless, they do exhibit two important differences with the galaxies lying above the MS.

First, they all exhibit a similar morphology in the H-band. They look like face-on disks, or, alternatively, like spheroids. Considering that the probability of seeing these galaxies only face-on is low, we believe that at least some of them are spheroids or will become so. This is at least the case of GS1 with an H-band Sérsic index of $n_H^{\rm Sersic} = 3.75$ and possibly also GS3 with $n_H^{\rm Sersic} = 2.03$ and $n_{ALMA}^{\rm Sersic} = 4.7 \pm 1.7$. Second, they all have small gas fractions more than twice lower than the galaxies lying above the MS.

The physical origin of these compact starbursts hidden in the MS is not completely clear at this stage. They experience such rapid star formation that they will exhaust their gas reservoirs and stop forming stars in only ∼150 Myr. Therefore, if they are not replenished by diffuse intergalactic matter, these massive galaxies will become passive. It has been debated whether $z \sim 2$ compact early-type galaxies (ETG) were the natural result of the global shrinking of galaxies going to higher redshifts or whether their existence could be seen as the signature of a "wet compaction" mechanism. The median 5000 Å effective radius (observed H-band) of $z \sim 2$ massive ETGs is indeed of only $R_e \sim 1$ kpc whereas the radii of star-forming galaxies in the same mass range is close to $R_e \sim 4$ kpc (see van der Wel et al. 2014 and references therein).

In a study of six massive, compact, dusty star-forming galaxies at $z \sim 2.5$ (including three galaxies in common with the present paper), Barro et al. (2016) proposed to explain compact dusty star-forming galaxies as galaxies experiencing a wet compaction event. Our analysis supports the idea that a mechanism is at play in a sub-population of $z \sim 2$ MS galaxies that leads to a strong concentration of their gas and dust reservoirs, associated with a drop of their depletion time.

The question of which physical mechanism produced this gas concentration remains open. Dekel & Burkert (2014) proposed to explain the wet compaction as a result of a violent disk instability (VDI) in a gas-rich system. However, more recent studies indicate that the effect of VDI alone may not be strong enough to generate such strong concentrations of gas. A violent mechanism, such as a major or a minor merger, appears to be required in most cases to strongly reduce the angular momentum (A. Dekel priv. comm. and paper in preparation). This was already coming out of the simulations presented in Zolotov et al. (2015) and Tacchella et al. (2016) although Tacchella et al. (2016) "find that the high-SFR galaxies in the upper envelope of the MS are compact, with high gas fractions and short depletion times ('blue nuggets')", whereas our compact MS galaxies exhibit lower gas fractions than typical MS galaxies.

The idea that mergers may affect MS galaxies without inducing strong starbursts is reinforced by the high-resolution hydrodynamic simulations of Fensch et al. (2017) showing that the SFR of two nearly equal-mass galaxies with 60% gas fractions (mimicking the large gas fractions of high-redshift galaxies) does not vary much during the merger event. Only a mild rise of the SFR by a factor 2.5 is observed at the late stage of the merger. The starbursts hidden in the MS could be explained by this phase in which the gas fraction has dropped and the SFR has risen without bringing the galaxy above the MS. The morphology of these compact star-forming galaxies is consistent with that of a spherical galaxy having lost its disk during the encounter. This would mean that mergers could be playing an important role in both triggering star formation and transforming disks into spheroids within the MS.

However, our sample of $z \sim 2$ MS galaxies is limited to massive galaxies with $M_\star > 10^{11}$ $M_\odot$. Because of this strong bias in favor of massive galaxies, we cannot generalize the existence of starbursts hidden in the MS to the full population of $z \sim 2$ galaxies. It is possible that these galaxies only exist in the very-high-mass end of the MS or are less important in relative fractions at lower masses. They may even represent a large fraction of the most massive galaxies at $z \sim 2$. Only deeper ALMA data will allow us to answer this question by probing the sizes of individual galaxies at lower stellar masses, knowing that the typical size of 5×10^{10} $M_\odot$ galaxies were found to be ∼5 kpc from stacking measurements (Lindroos et al. 2016). At this stage, it is entirely possible that this mechanism is typical of massive galaxies only and as such it may be more directly linked to the mass of the galaxies than to a recent major merger.

Lastly, we are left with the following question regarding starbursts above the MS. If major mergers of gas-rich systems do not produce starbursts, then why do we see starbursts at all at $z \sim 2$? The answer to this question may be found in the gas fraction measured in starbursts. As we showed in Fig. 13 and as discussed in, for example, Tacconi et al. (2018), starbursts are not only forming stars efficiently, they exhibit an equivalently strong excess in their gas fraction. In that sense, they are different from the late-stage merger phase that we discussed above if their enhanced gas content is not artificially created by an underestimation of their metallicity (underestimating the metallicity of a dusty starburst would imply underestimating their dust-to-gas ratio and therefore overestimating their gas mass). A possible explanation for these gas enriched starbursts could be that they are fed by the infall of circum-galactic material induced during the merger in some specific conditions. How else can one understand that two galaxies with a given gas fraction end up forming a merged system with a higher gas fraction? Idealized hydrodynamic simulations would be needed in order to determine if indeed there exists specific conditions that may induce an efficient infall of circum-galactic matter during a major merger. To our knowledge, simulations that would allow a quantitative comparison of the same merger conditions with and without circum-galactic matter do not exist at present. Such simulations should be performed to study the effects of circum-galactic gas and its possible infall during a merger. Simulations in full cosmological context naturally include intergalactic infall (e.g., Martin et al. 2017) but lack comparison cases of galaxies in the exact same conditions with and without a circum-galactic reservoir of gas.

5. Conclusions

In this paper, we present the properties of a sample of 19 $z \sim 2$ star-forming galaxies located in the GOODS-*South* field with high-angular-resolution imaging and photometry from the UV to the millimeter range, combining data from the ground, HST, *Spitzer*, *Herschel*, and ALMA: the ALMA data combine information from deep integrations at 870 μm on 8 $z \sim 2$ sources selected among the brightest *Herschel* sources with data on 11 galaxies coming from a published 1.3 mm survey of the *Hubble* Ultra-Deep Field, HUDF (Dunlop et al. 2017; Rujopakarn et al. 2016). These galaxies were selected in the high stellar mass range of the star-forming galaxies at $1.5 < z < 2.5$ in order to include normal star-forming galaxies within the standard deviation of the star formation MS, as well as starbursts well above the MS.

Heavily obscured $z \sim 2$ massive galaxies: out of eight ALMA pointings targeting *Herschel* sources with an optical counterpart at $z \sim 2$, one of the ALMA detection presents two properties

that led us to identify a background HST-dark galaxy as the real *Herschel* and ALMA counterpart. These properties are (i) an offset between ALMA and HST larger than the astrometric error, and (ii) a FIR SED that peaks at $\sim 400\,\mu$m. We identified a potential counterpart at a redshift that we estimate to be $z \sim 3.24$. A 67 armcin^2 survey of GOODS-*South* at 1.1 mm (P.I.D. Elbaz) appears to confirm the possibility that typically 10–15% of the ALMA sources are associated with "optically dark" galaxies (Franco et al. 2018).

Compact star-formation in $z \sim 2$ massive galaxies: while dusty star-formation is resolved in all ALMA galaxies, we find a common point among these massive $z \sim 2$ star-forming galaxies: their star formation appears to be concentrated towards the mass center of the galaxies and to be 1.45 ± 1.0 times more compact than at $1.6\,\mu$m, that is, the observed HST–WFC3 H-band.

Minor contribution of kiloparsec-size clumps of star formation: kiloparsec-size clumps of star formation seen in the UV do not contribute a large fraction of the total SFR measured in these massive $z \sim 2$ galaxies. This is consistent with the small SFR attributed to the giant UV clumps (see Elmegreen et al. 2009). In one case, we see marginal evidence for the ALMA detection of a kiloparsec-size clump.

The IR8 color index as a probe of star-formation compactness: we present an updated version of the $IR8$-$\Sigma_{\rm IR}$ relation (introduced in Elbaz et al. 2011) for local galaxies, now including resolved *Herschel* images for local galaxies, and discuss its extension to $z \sim 2$. The $IR8$ color index ($= L_{\rm IR}/L_8$) and the IR luminosity surface density, $\Sigma_{\rm IR}$ (a proxy for the dusty star formation density) present a tight correlation for local galaxies with a standard deviation of only RMS = 0.11 dex. The $z \sim 1.5$–2.5 galaxies resolved with ALMA appear to follow the local relation, although galaxies both within and above the MS can exhibit high $\Sigma_{\rm IR}$ values.

A connection between AGN activity and star-formation compactness: galaxies hosting an AGN appear to be outliers to the $IR8$-$\Sigma_{\rm IR}$ relation both locally and at $z \sim 2$. While a correction of the contribution of hot dust continuum due to AGN heating may explain in part or possibly completely the position of these galaxies, by lowering their $IR8$, galaxies hosting an AGN are found to be systematically associated with the most compact star-forming galaxies. This suggests that the mechanism responsible for the most compact star-forming galaxies also switches on the AGN, or possibly that the AGN plays a role in triggering the compact star-formation through positive feedback (see e.g., Elbaz et al. 2009; Silk 2013; Molnár et al. 2017).

Investigating the origin of merger-driven starbursts above the star formation main sequence: galaxies above the SFR-M$_\star$ MS systematically exhibit the visual morphology of perturbed galaxies as expected in the case of major mergers. We confirm that their increased efficiency of star formation is accompanied with a rise of their gas fraction. If it is not artificially created by a larger metallicity in starbursts (which would lead to an overestimate of their gas content), this increase in gas content may be explained by the infall of circum-galactic material induced during the merger in some specific conditions that remain to be determined.

Compact starbursts hidden in the high-mass end of the MS: we find that the depletion time, $\tau_{\rm dep}$ (the time for a galaxy to consume its molecular gas reservoir), drops with increasing IR luminosity surface density, $\Sigma_{\rm IR}$. The galaxies with the shortest depletion times ($\tau_{\rm dep} \sim 150$ Myr) and highest IR luminosity surface densities ($\Sigma_{\rm IR} \sim 1.5 \times 10^{12}\ L_\odot\ {\rm kpc}^{-2}$) are massive galaxies ($M_\star > 10^{11}\ M_\odot$) dominantly located in the upper part of the MS; these are therefore starbursts "hidden" within the MS. Due to our *Herschel* selection, we do not know whether similar galaxies exist at lower masses, and therefore these compact starbursts in the MS may represent the late stage of star formation in massive galaxies before their passivization. The low gas fraction of these galaxies also favors the possibility that they are experiencing a last stage of star formation prior to becoming passive. The physical origin of the compact starbursts within the MS remains uncertain at this stage. Understanding it will be crucial in the future to unveiling the origin of the compactness of the stars of early-type galaxies observed at $z \sim 2$.

Starburstiness and star-formation compactness measure the incorrectness of UV-corrected SFR: we present a near proportionality between the ratio of SFR$_{\rm tot}$ ($= {\rm SFR_{IR}} + {\rm SFR_{UV}}$) over SFR$_{\rm SED}$ (determined by fitting the rest-frame UV-optical-NIR) and the distance to the MS or starburstiness ($R_{\rm SB} = {\rm SFR_{tot}/SFR_{MS}}$). Therefore, SED-fitting underestimates the SFR with increasing starburstiness. This can be explained by the fact that the regions responsible for the bulk of rest-frame UV and FIR emission occupy very distinct locations in starbursts as shown by our ALMA images. Interestingly, this is also the case of the "starbursts hidden in the MS", that is, MS galaxies experiencing compact star formation and short depletion times. This suggests that SFR derived from SED-fitting will most probably miss this population which may be a problem when searching for causes of star-formation variations such as environment effects.

Acknowledgements. This paper makes use of the following ALMA data: ADS/JAO.ALMA#2012.1.00983.S. ALMA is a partnership of ESO (representing its member states), NSF (USA) and NINS (Japan), together with NRC (Canada), MOST and ASIAA (Taiwan), and KASI (Republic of Korea), in cooperation with the Republic of Chile. The Joint ALMA Observatory is operated by ESO, AUI/NRAO and NAOJ. R.L. acknowledges support from Comité Mixto ESO-GOBIERNO DE CHILE, GEMINI-CONICYT FUND 32130024, FONDECYT Grant 3130558, and CEA-Saclay. This research was supported by the French Agence Nationale de la Recherche (ANR) project ANR-09-BLAN-0224. DE acknowledges the contribution of the FP7 SPACE project ASTRODEEP (Ref. No: 312725), supported by the European Commission. We acknowledge financial support from the "Programme National de Cosmologie et des Galaxies" (PNCG) of CNRS/INSU, France. GEM acknowledges support from the Carlsberg Foundation, the ERC Consolidator Grant funding scheme (project ConTExt, grant number No. 648179), and a research grant (13160) from Villum Fonden. W.R. is supported the Thailand Research Fund/Office of the Higher Education Commission Grant Number MRG6080294. T.D-S. acknowledges support from ALMA-CONICYT project 31130005 and FONDECYT regular project 1151239.

References

Abel, N. P., Dudley, C., Fischer, J., Satyapal, S., & van Hoof, P. A. M. 2009, ApJ, 701, 1147
Allamandola, L. J., Tielens, A. G. G. M., & Barker, J. R. 1985, ApJ, 290, L25
Armus, L., Mazzarella, J. M., Evans, A. S., et al. 2009, PASP, 121, 559
Barro, G., Kriek, M., Pérez-González, P. G., et al. 2016, ApJ, 827, L32
Béthermin, M., Daddi, E., Magdis, G., et al. 2015, A&A, 573, A113
Brammer, G. B., van Dokkum, P. G., & Coppi, P. 2008, ApJ, 686, 1503
Bruzual, G., & Charlot, S. 2003, MNRAS, 344, 1000
Buat, V., Noll, S., Burgarella, D., et al. 2012, A&A, 545, A141
Burgarella, D., Buat, V., Gruppioni, C., et al. 2013, A&A, 554, A70
Calzetti, D., Armus, L., Bohlin, R. C., et al. 2000, ApJ, 533, 682
Chambers, K. C., Magnier, E. A., Metcalfe, N., et al. 2016, ArXiv e-prints [arXiv:1612.05560]
Chang, Y.-Y., Le Floc'h, E., Juneau, S., et al. 2017a, MNRAS, 466, L103
Chang, Y.-Y., Le Floc'h, E., Juneau, S., et al. 2017b, ApJS, 233, 19
Chary, R., & Elbaz, D. 2001, ApJ, 556, 562
Cibinel, A., Daddi, E., Bournaud, F., et al. 2017, MNRAS, 469, 4683
Cowie, L. L., Hu, E. M., & Songaila, A. 1995, AJ, 110, 1576
Daddi, E., Cimatti, A., Renzini, A., et al. 2004, ApJ, 617, 746
Daddi, E., Dickinson, M., Morrison, G., et al. 2007, ApJ, 670, 156

Daddi, E., Bournaud, F., Walter, F., et al. 2010a, ApJ, 713, 686
Daddi, E., Elbaz, D., Walter, F., et al. 2010b, ApJ, 714, L118
Daddi, E., Dannerbauer, H., Liu, D., et al. 2015, A&A, 577, A46
Dekel, A., & Burkert, A. 2014, MNRAS, 438, 1870
Díaz-Santos, T., Charmandaris, V., Armus, L., et al. 2010, ApJ, 723, 993
Díaz-Santos, T., Armus, L., Charmandaris, V., et al. 2017, ApJ, 846, 32
Donley, J. L., Koekemoer, A. M., Brusa, M., et al. 2012, ApJ, 748, 142
Draine, B. T., & Li, A. 2007, ApJ, 657, 810
Draine, B. T., Dale, D. A., Bendo, G., et al. 2007, ApJ, 663, 866
Dunlop, J. S., McLure, R. J., Biggs, A. D., et al. 2017, MNRAS, 466, 861
Elbaz, D., Daddi, E., Le Borgne, D., et al. 2007, A&A, 468, 33
Elbaz, D., Jahnke, K., Pantin, E., Le Borgne, D., & Letawe, G. 2009, A&A, 507, 1359
Elbaz, D., Hwang, H. S., Magnelli, B., et al. 2010, A&A, 518, L29
Elbaz, D., Dickinson, M., Hwang, H. S., et al. 2011, A&A, 533, A119
Elmegreen, B. G., & Elmegreen, D. M. 2005, ApJ, 627, 632
Elmegreen, B. G., Bournaud, F., & Elmegreen, D. M. 2008, ApJ, 688, 67
Elmegreen, B. G., Elmegreen, D. M., Fernandez, M. X., & Lemonias, J. J. 2009, ApJ, 692, 12
Erb, D. K., Shapley, A. E., Pettini, M., et al. 2006, ApJ, 644, 813
Erwin, P. 2015, ApJ, 799, 226
Fensch, J., Renaud, F., Bournaud, F., et al. 2017, MNRAS, 465, 1934
Flewelling, H. A., Magnier, E. A., Chambers, K. C., et al. 2016, ArXiv e-prints [arXiv:1612.05243]
Fontana, A., Dunlop, J. S., Paris, D., et al. 2014, A&A, 570, A11
Franco, M., Elbaz, D., Béthermin, M., et al. 2018, A&A, accepted [arXiv:1803.00157]
Fujimoto, S., Ouchi, M., Shibuya, T., & Nagai, H. 2017, ApJ, 850, 83
Genzel, R., Tacconi, L. J., Combes, F., et al. 2012, ApJ, 746, 69
Genzel, R., Tacconi, L. J., Lutz, D., et al. 2015, ApJ, 800, 20
Guo, Y., Ferguson, H. C., Giavalisco, M., et al. 2013, ApJS, 207, 24
Heinis, S., Buat, V., Béthermin, M., et al. 2013, MNRAS, 429, 1113
Hodge, J. A., Swinbank, A. M., Simpson, J. M., et al. 2016, ApJ, 833, 103
Hopkins, P. F., Bundy, K., Croton, D., et al. 2010, ApJ, 715, 202
Karim, A., Schinnerer, E., Martínez-Sansigre, A., et al. 2011, ApJ, 730, 61
Kartaltepe, J. S., Sanders, D. B., Scoville, N. Z., et al. 2007, ApJS, 172, 320
Kennicutt, Jr. R. C. 1998, ApJ, 498, 541
Kriek, M., van Dokkum, P. G., Labbé, I., et al. 2009, ApJ, 700, 221
Le Floc'h, E., Papovich, C., Dole, H., et al. 2005, ApJ, 632, 169
Leger, A., & Puget, J. L. 1984, A&A, 137, L5
Leiton, R., Elbaz, D., Okumura, K., et al. 2015, A&A, 579, A93
Leroy, A. K., Bolatto, A., Gordon, K., et al. 2011, ApJ, 737, 12
Lindroos, L., Knudsen, K. K., Fan, L., et al. 2016, MNRAS, 462, 1192
Luo, B., Brandt, W. N., Xue, Y. Q., et al. 2017, ApJS, 228, 2
Madau, P., & Dickinson, M. 2014, ARA&A, 52, 415
Magdis, G. E., Daddi, E., Béthermin, M., et al. 2012a, ApJ, 760, 6
Magdis, G. E., Daddi, E., Sargent, M., et al. 2012b, ApJ, 758, L9
Magnelli, B., Elbaz, D., Chary, R. R., et al. 2009, A&A, 496, 57
Magnelli, B., Popesso, P., Berta, S., et al. 2013, A&A, 553, A132
Martin, G., Kaviraj, S., Devriendt, J. E. G., et al. 2017, MNRAS, 472, L50
Meurer, G. R., Heckman, T. M., & Calzetti, D. 1999, ApJ, 521, 64
Molnár, D. C., Sargent, M. T., Elbaz, D., Papadopoulos, P. P., & Silk, J. 2017, MNRAS, 467, 586
Mullaney, J. R., Alexander, D. M., Goulding, A. D., & Hickox, R. C. 2011, MNRAS, 414, 1082
Noeske, K. G., Weiner, B. J., Faber, S. M., et al. 2007, ApJ, 660, L43
Noll, S., Burgarella, D., Giovannoli, E., et al. 2009, A&A, 507, 1793
Overzier, R. A., Heckman, T. M., Wang, J., et al. 2011, ApJ, 726, L7
Pannella, M., Carilli, C. L., Daddi, E., et al. 2009, ApJ, 698, L116
Pannella, M., Elbaz, D., Daddi, E., et al. 2015, ApJ, 807, 141
Peng, C. Y., Ho, L. C., Impey, C. D., & Rix, H.-W. 2002, AJ, 124, 266
Puglisi, A., Daddi, E., Renzini, A., et al. 2017, ApJ, 838, L18
Reddy, N., Dickinson, M., Elbaz, D., et al. 2012, ApJ, 744, 154
Renzini, A., & Peng, Y.-j. 2015, ApJ, 801, L29
Rodighiero, G., Daddi, E., Baronchelli, I., et al. 2011, ApJ, 739, L40
Rodighiero, G., Renzini, A., Daddi, E., et al. 2014, MNRAS, 443, 19
Rujopakarn, W., Rieke, G. H., Eisenstein, D. J., & Juneau, S. 2011, ApJ, 726, 93
Rujopakarn, W., Dunlop, J. S., Rieke, G. H., et al. 2016, ApJ, 833, 12
Salpeter, E. E. 1955, ApJ, 121, 161
Schreiber, C., Pannella, M., Elbaz, D., et al. 2015, A&A, 575, A74
Schreiber, C., Pannella, M., Leiton, R., et al. 2017, A&A, 599, A134
Shivaei, I., Reddy, N. A., Shapley, A. E., et al. 2017, ApJ, 837, 157
Silk, J. 2013, ApJ, 772, 112
Silverman, J. D., Daddi, E., Rodighiero, G., et al. 2015, ApJ, 812, L23
Simpson, J. M., Smail, I., Swinbank, A. M., et al. 2015, ApJ, 799, 81
Tacchella, S., Dekel, A., Carollo, C. M., et al. 2016, MNRAS, 457, 2790
Tacconi, L. J., Genzel, R., Neri, R., et al. 2010, Nature, 463, 781
Tacconi, L. J., Genzel, R., Saintonge, A., et al. 2018, ApJ, 853, 179
Tadaki, K.-i., Genzel, R., Kodama, T., et al. 2017, ApJ, 834, 135
van der Wel, A., Bell, E. F., Häussler, B., et al. 2012, ApJS, 203, 24
van der Wel, A., Franx, M., van Dokkum, P. G., et al. 2014, ApJ, 788, 28
Whitaker, K. E., van Dokkum, P. G., Brammer, G., & Franx, M. 2012, ApJ, 754, L29
Whitaker, K. E., Franx, M., Leja, J., et al. 2014, ApJ, 795, 104
Wuyts, S., Förster Schreiber, N. M., Lutz, D., et al. 2011a, ApJ, 738, 106
Wuyts, S., Förster Schreiber, N. M., van der Wel, A., et al. 2011b, ApJ, 742, 96
Zolotov, A., Dekel, A., Mandelker, N., et al. 2015, MNRAS, 450, 2327